

NGTS-EB-7, an eccentric, long-period, low-mass eclipsing binary

Toby Rodel¹ ^{*}, Christopher. A. Watson¹ , Solène Ulmer-Moll^{2,3} , Samuel Gill^{4,5} , Pierre F. L. Maxted⁶ , Sarah L. Casewell⁷ , Rafael Brahm^{8,9,10} , Thomas G Wilson^{4,5} , Jean C. Costes¹, Yoshi Nike Emilia Eschen^{4,5} , Lauren Doyle^{4,5} , Alix V. Freckelton¹¹ , Douglas R. Alves^{12,13} , Ioannis Apergis^{4,5} , Daniel Bayliss^{4,5} , Francois Bouchy² , Matthew R. Burleigh⁷ , Xavier Dumusque² , Jan Eberhardt¹⁴ , Jorge Fernández Fernández^{4,5} , Edward Gillen¹⁵ , Michael R. Goad⁷ , Faith Hawthorn^{4,5} , Ravit Helled¹⁶ , Thomas Henning¹⁴, Katlyn L. Hobbs¹ , James S. Jenkins^{17,13} , Andrés Jordán^{9,8,10} , Alicia Kendall⁷ , Monika Lendl² , James McCormac^{4,5} , Ernst J.W. de Mooij¹ , Sean M. O’Brien¹ , Suman Saha^{17,13} , Marcelo Tala Pinto^{9,8} , Trifon Trifonov^{18,19} , Stéphane Udry² , Peter J. Wheatley^{4,5} 

¹*Astrophysics Research Centre, School of Mathematics and Physics, Queen’s University Belfast, Belfast, BT7 1NN, UK*

²*Observatoire de Genève, Université de Genève, 51 Ch. des Maillettes, CH-1290 Sauverny, Switzerland*

³*Space Research and Planetary Sciences, Physics Institute, University of Bern, Gesellschaftsstrasse 6, 3012 Bern, Switzerland*

⁴*Department of Physics, University of Warwick, Gibbet Hill Road, Coventry CV4 7AL, UK*

⁵*Centre for Exoplanets and Habitability, University of Warwick, Gibbet Hill Road, Coventry CV4 7AL, UK*

⁶*Astrophysics Group, Keele University, Keele, Staffordshire ST5 5BG, UK*

⁷*School of Physics and Astronomy, University of Leicester, Leicester LE1 7RH, UK*

⁸*Millennium Institute of Astrophysics (MAS), Nuncio Monseñor Sótero Sanz 100, Providencia, Santiago, Chile*

⁹*Facultad de Ingeniería y Ciencias, Universidad Adolfo Ibáñez, Av. Diagonal Torres, Peñalolén 2640, Santiago, Chile*

¹⁰*Data Observatory Foundation, Eliodoro Yáñez 2990, Providencia, Santiago, Chile*

¹¹*School of Physics & Astronomy, University of Birmingham, Edgbaston, Birmingham B15 2TT, UK*

¹²*Departamento de Astronomía, Universidad de Chile, Casilla 36-D, Santiago, Chile*

¹³*Centro de Excelencia en Astrofísica y Tecnologías Afines (CATA), Camino El Observatorio 1515, Las Condes, Santiago, Chile*

¹⁴*Max-Planck-Institut für Astronomie, Königstuhl 17, 69117 Heidelberg, Germany*

¹⁵*Astronomy Unit, Queen Mary University of London, Mile End Road, London E1 4NS, UK*

¹⁶*Department of Astrophysics, University of Zurich, Winterthurerstr. 190, 8057 Zurich, Switzerland*

¹⁷*Instituto de Estudios Astrofísicos, Facultad de Ingeniería y Ciencias, Universidad Diego Portales, Av. Ejército Libertador 441, Santiago, Chile*

¹⁸*Landessternwarte, Zentrum für Astronomie der Universität Heidelberg, Königstuhl 12, 69117 Heidelberg, Germany*

¹⁹*Department of Astronomy, Sofia University St Kliment Ohridski, 5 James Bourchier Blvd, BG-1164 Sofia, Bulgaria*

Accepted XXX. Received YYY; in original form ZZZ

ABSTRACT

Despite being the most common types of stars in the Galaxy, the physical properties of late M dwarfs are often poorly constrained. A trend of radius inflation compared to evolutionary models has been observed for earlier type M dwarfs in eclipsing binaries, possibly caused by magnetic activity. It is currently unclear whether this trend also extends to later type M dwarfs below the convective boundary. This makes the discovery of lower-mass, fully convective, M dwarfs in eclipsing binaries valuable for testing evolutionary models – especially in longer-period binaries where tidal interaction between the primary and secondary is negligible. With this context, we present the discovery of the NGTS-EB-7 AB system, an eclipsing binary containing a late M dwarf secondary and an evolved G-type primary star. The secondary star has a radius of $0.125 \pm 0.006 R_{\odot}$, a mass of $0.096^{+0.003}_{-0.004} M_{\odot}$ and follows a highly eccentric ($e=0.71436 \pm 0.00085$) orbit every 193.35875 ± 0.00034 days. This makes NGTS-EB-7 AB the third longest-period eclipsing binary system with a secondary smaller than $200 M_J$ with the mass and radius constrained to better than 5%. In addition, NGTS-EB-7 is situated near the centre of the proposed LOPS2 southern field of the upcoming PLATO mission, allowing for detection of the secondary eclipse and measurement of the companion’s temperature. With its long-period and well-constrained physical properties - NGTS-EB-7 B will make a valuable addition to the sample of M dwarfs in eclipsing binaries and help in determining accurate empirical mass/radius relations for later M dwarf stars.

Key words: stars: binaries: eclipsing – stars: fundamental properties – stars: late type – stars: low mass – planets and satellites: detection – planets and satellites: fundamental properties

* Email: trodel01@qub.ac.uk

1 INTRODUCTION

In recent years late M dwarfs have become attractive targets for exoplanet surveys attempting to find temperate Earth-sized planets. The small radii and masses of M dwarfs means an Earth-sized planet produces deeper transits and induces a larger amplitude reflex motion on its host star relative to higher-mass stars, both of which allow for easier detection. Additionally, the cooler temperatures of late M dwarfs coupled to their small radii (and therefore lower luminosities) means that the ‘temperate zone’ is much closer to the star than it would be around a solar-type star. Since closer-in planets are easier to detect with both transits and radial velocities, this makes detection of temperate (and thus potentially habitable) planets more likely around late M dwarfs than earlier type stars. These factors have led to large scale surveys such as M_{Earth} (Nutzman et al. 2009) and the Search for habitable Planets Eclipsing ULtra-cOOl Stars (*SPECULOOS*; Sebastian et al. 2021) being dedicated entirely to searching for planets around M dwarfs and other large surveys such as the Transiting Exoplanet Survey Satellite (*TESS*; Ricker et al. 2015) prioritising nearby M dwarfs as targets. Such survey efforts have already led to exciting discoveries, including a compact system of 7 planets (up to 4 of which are potentially temperate) similar in size to Earth orbiting the M8V (Costa et al. 2006) star *TRAPPIST-1* (Gillon et al. 2017).

In order to obtain accurate planetary parameters, the host star itself must first be accurately characterised. However, there has been a long-observed discrepancy between the theoretical masses and radii from evolutionary models and the measured masses and radii of M dwarfs in eclipsing binaries – which was identified as early as Hoxie (1970). Studies such as Spada et al. (2013) and Parsons et al. (2018) have found M dwarf binary companions are often cooler and larger than predicted by models by a factor of 3–10%. There is currently conflicting evidence for whether this ‘radius inflation problem’ is confined to earlier type M dwarfs between $0.35 M_{\odot}$ and $0.5 M_{\odot}$ or whether it also extends to fully convective later type M dwarfs below $0.35 M_{\odot}$. Parsons et al. (2018) found that radius inflation was present either side of the convective boundary, while von Boetticher et al. (2019) instead recovered a strong radius dependence on metallicity for fully convective companions and that any systematic radius inflation was highly model dependent. The discovery and precise characterisation of more late M dwarfs transiting bright F, G or K dwarf stars in Eclipsing Binary - Low Mass (EBLM; Triaud et al. 2013; Gómez Maqueo Chew et al. 2014; von Boetticher et al. 2017; Triaud et al. 2017; von Boetticher et al. 2019; Gill et al. 2019; Kunovac Hodžić et al. 2020; Swayne et al. 2021; Sebastian et al. 2023; Duck et al. 2023; Maxted et al. 2023; Swayne et al. 2024; Davis et al. 2024; Sebastian et al. 2024) systems is vital to understand why the radius inflation problem exists and whether it extends below the convective boundary.

Many of the models proposed rely on magnetic effects to explain the larger than expected radii of M dwarfs (Mullan & MacDonald 2001; Chabrier et al. 2007; López-Morales 2007; MacDonald & Mullan 2014; Morales et al. 2022). The majority of EBLMs have short orbital periods (over 70% of the sample from Maxted et al. (2023) have orbital periods <10 days) and hence their orbital separations are relatively small. In such short-period systems, tidal interactions with the primary are expected to synchronise the rotation of the M dwarf secondary to its orbit, causing it to spin much faster than a typical M-dwarf. This increases the magnetic field strength of the secondary, leading to an inflated radius. However, studies of longer-period M dwarfs have already found conflicting results of how the binary period may affect the radius. For example, von Boetticher

et al. (2019) found no relation between orbital period and radius inflation, while Swayne et al. (2024) found shorter period binaries were more inflated. However, both of these studies were performed on relatively small samples of M dwarf binary companions with few having periods longer than 30 days. Thus, to accurately understand radius inflation, a larger sample of longer-period fully convective M dwarf binary companions is required.

It is in this context that we present the discovery of TIC 238060327 B; a late M dwarf similar in mass and radius to *TRAPPIST-1* on a highly eccentric ~ 193 day orbit with an evolved G type star. Henceforth, we refer to the system as *NGTS-EB-7* (see Appendix F and Table F1 for more information on this naming system). In Section 2 we describe the photometric observations that led to the discovery of *NGTS-EB-7 B* and in Section 3 we describe the spectroscopic observations used to characterise the primary star and to confirm the presence of the secondary companion by radial velocity measurement. In Section 4 we describe the techniques used to analyse the spectra in order to characterise the primary and in Section 5 we describe how we fit an orbital solution to the system to obtain parameters for the secondary. In Section 6 we present the results of our analysis and discuss the nature of the system and its implications for further study of late M dwarfs. Finally, in Section 7 we summarise the work so far and close with some remarks on potential future work on this system.

2 PHOTOMETRIC OBSERVATIONS

In this section we describe the photometric observations from the Transiting Exoplanet Survey Satellite (*TESS*; Ricker et al. 2015, Section 2.1) and the Next Generation Transit Survey (*NGTS*; Wheatley et al. 2018, Section 2.2) that led to the discovery of *NGTS-EB-7 B*. These observations are summarised in Table 1.

2.1 TESS

The Transiting Exoplanet Survey Satellite (*TESS*; Ricker et al. 2015), is a space-based all-sky survey searching for transiting planets around nearby bright stars. The *TESS* spacecraft has a payload of 4 onboard cameras each consisting of four CCDs. The cameras are arranged in a vertical configuration, resulting in a rectangular field of view. Since 2018, *TESS* has been performing a near all-sky survey by rotating its pointings around the ecliptic poles at regular intervals, with each different pointing referred to as a sector. *TESS* observes each $24^{\circ} \times 96^{\circ}$ sector for ~ 27 days at a time, although some targets have longer observation baselines due to the overlapping regions between sectors closer to the ecliptic poles.

NGTS-EB-7 was observed by *TESS* in the Full Frame Images (FFIs) of sectors 6, 7 and 8 at 30-minute cadence; sectors 29, 33, 34, 35 and 39 at 10-minute cadence; and sectors 61, 62 and 66 at 200-second cadence. Sectors 6 to 39 have lightcurves produced from the FFIs by the *TESS* Science Processing Operations Centre (*TESS-SPOC*; Jenkins et al. 2016; Caldwell et al. 2020) pipeline and those for Sectors 61, 62 and 66 are produced by the Quick Look Pipeline (QLP; Huang et al. 2020). A summary of the *TESS* lightcurves and other photometric data, including observation dates, is given in Table 1 and the lightcurves are shown in Figure E1. Most of the lightcurves appear relatively featureless with the exception of the transit features in Sector 8 and in the high scattered light region of Sector 29 (this scattered light is removed from the other sectors by detrending). In addition, the Sector 39 lightcurve shows high correlated noise, likely due to spacecraft jitter. Note that we remove any timestamps with

Table 1. Summary of the photometric observations for *NGTS-EB-7*.

Instrument	Night(s) Observed	N_{images}	Exptime (s)	Filter	TESS Sector	Comments
<i>TESS</i>	2018/12/12-2019/01/06	973	1800	<i>TESS</i>	6	
<i>TESS</i>	2019/01/08-2019/02/01	1081	1800	<i>TESS</i>	7	
<i>TESS</i>	2019/02/02-2019/02/27	807	1800	<i>TESS</i>	8	Transit
<i>TESS</i>	2020/08/26-2020/09/21	3572	600	<i>TESS</i>	29	Transit in ramp
<i>TESS</i>	2020/12/18-2021/01/13	3485	600	<i>TESS</i>	33	
<i>TESS</i>	2021/01/14-2021/02/08	3347	600	<i>TESS</i>	34	
<i>TESS</i>	2021/02/09-2021/03/06	2711	600	<i>TESS</i>	35	
<i>TESS</i>	2021/05/27-2021/06/24	3864	600	<i>TESS</i>	39	
<i>TESS</i>	2023/01/18-2023/02/12	9328	200	<i>TESS</i>	61	Quick Look Pipeline only
<i>TESS</i>	2023/02/12-2023/03/10	10273	200	<i>TESS</i>	62	Quick Look Pipeline only
<i>TESS</i>	2023/06/02-2023/07/01	10098	200	<i>TESS</i>	66	Quick Look Pipeline only
<i>NGTS</i>	2022/04/09-2022/06/09	5088	10	<i>NGTS</i>	N/A	Initial monitoring
<i>NGTS</i>	2022/10/19, 2023/02/25, 2023/03/25	4145	10	<i>NGTS</i>	N/A	Targeted followup
<i>NGTS</i>	2023/11/10	8813	2	<i>NGTS</i>	N/A	Egress

flux values of NaN or with a data quality flag not equal to zero (with the exception of sector 29 where a transit occurs near the end of a *TESS* orbit in a region of high scattered light).

A single transit of *NGTS-EB-7 B* was detected by a custom single-transit search algorithm, as described in Gill et al. (2020), in the Sector 8 *TESS*-SPOC FFI lightcurve at TBJD=1519.3. The Sector 8 *TESS*-SPOC FFI lightcurve containing the transit is shown in Figure 1a. A second transit occurred in sector 29 but was not visible in the *TESS*-SPOC lightcurve PDCSAP Flux due to scattered light from the Earth at the end of the orbit. To remove the scattered light, we used the `RegressionCorrector` class from the `Lightkurve` (`Lightkurve Collaboration et al. 2018`) package for Python. The `RegressionCorrector` class uses a ‘design matrix’, made up of the flux from all pixels outside of the aperture with an offset term in order to fit the mean level of the lightcurve. This is done under the assumption that pixels outside the aperture will contain no flux from the target. The lightcurve is then detrended against all of these vectors to produce a model of the mean flux. The resulting model flux is subtracted from itself at the fifth percentile to avoid reducing the flux below zero before being subtracted from the uncorrected lightcurve, resulting in a lightcurve corrected for scattered light. This allowed us to produce a lightcurve from the *TESS*-SPOC FFI target pixel file (`tpf`) with the scattered light corrected for in order to reveal the transit event - which is shown in Figure 1b.

2.2 NGTS

The Next Generation Transit Survey (*NGTS*; Wheatley et al. 2018) is a facility made up of 12 independent robotic telescopes with 20-cm apertures located in Paranal, Chile. The high photometric precision of *NGTS*, which can rival or even exceed that of *TESS* from the ground (Bryant et al. 2020; Bayliss et al. 2022; O’Brien et al. 2022), makes it well suited for follow-up of single transit events from *TESS*, as described in Bayliss et al. (2020).

Following the detection of the initial transit in *TESS* Sector 8 (see Section 2.1), *NGTS-EB-7* was initially monitored by *NGTS* with 10-s exposures on 15 nights from 2022/04/09 to 2022/06/09. After solving the system (see Section 5.1) a transit was predicted to occur on the night of 2022-04-09. However one was not detected, this is because the observation window only covered the mid transit time with no ingress or egress observed. After the second *TESS* transit was observed, the period could be reduced to a set of discrete aliases, each an integer fraction of the time between the first and second *TESS* transits. *NGTS-EB-7* was set up for targeted monitoring with

NGTS to try and observe possible period aliases on the nights of 2022/10/19, 2023/02/25, 2023/03/25 and 2023/11/10. No transits were seen on 2023/02/25 or 2023/03/25. Similarly to the first set of observations, a mid transit with no baseline was observed on the night of 2022/10/19 - leading to another non-detection. Neither of these nights were included in the final transit fit (see Section 5.1). Details of this monitoring are set out in Table 1.

A transit egress and baseline of *NGTS-EB-7 B* was observed for 5.6 hours on the night of 2023/11/10. The event was consistent with the events seen in *TESS* for shape and depth. The event confirmed the orbital period of the system to be $P \approx 193$ days. We binned the *NGTS* data into 63 bins equally spaced in time with a resulting cadence of 300 s. The binned lightcurve is shown in Figure 1c.

3 SPECTROSCOPIC OBSERVATIONS

In this section we describe the spectroscopic measurements of *NGTS-EB-7* from *CORALIE* (Queloz et al. 2001, Section 3.1), the High Accuracy Radial-velocity Planet Searcher (*HARPS*; Mayor et al. 2003, Section 3.2) and the Fiberfed Extended Range Optical Spectrograph (*FEROS*; Kaufer et al. 1999), that were used to characterise the primary star and confirm the presence of *NGTS-EB-7 B* via radial velocity (RV) measurements. The RV measurements from both instruments can be found in Table 2.

3.1 CORALIE

We used the *CORALIE* (Queloz et al. 2001) fiber fed echelle spectrograph installed on the 1.2-m Leonhard Euler telescope at ESO La Silla Observatory to take radial velocity measurements of *NGTS-EB-7* between the nights of 2021/11/28 and 2023/02/27. A total of 21 spectra were taken within this timeframe. Most of the spectra were taken with an exposure time of 2100 s with airmasses between 1.46 and 1.08 although an exposure time of 1500 s was used on 4 nights and 1800 s on one night. The signal-to-noise ratio (SNR) of order 62 for these spectra ranges between 5.9 and 15.3, leading to an RV precision ranging between 20 and 60 m s⁻¹. The data were reduced using the standard *CORALIE* data reduction system (DRS 3.8) with a G2 mask used for cross-correlation. The data are set out in Table 2. These data revealed a large amplitude radial velocity variation in phase with the photometric transit signal. The radial velocity data and best-fitting model (as described in Section 5.1) are shown in Fig-

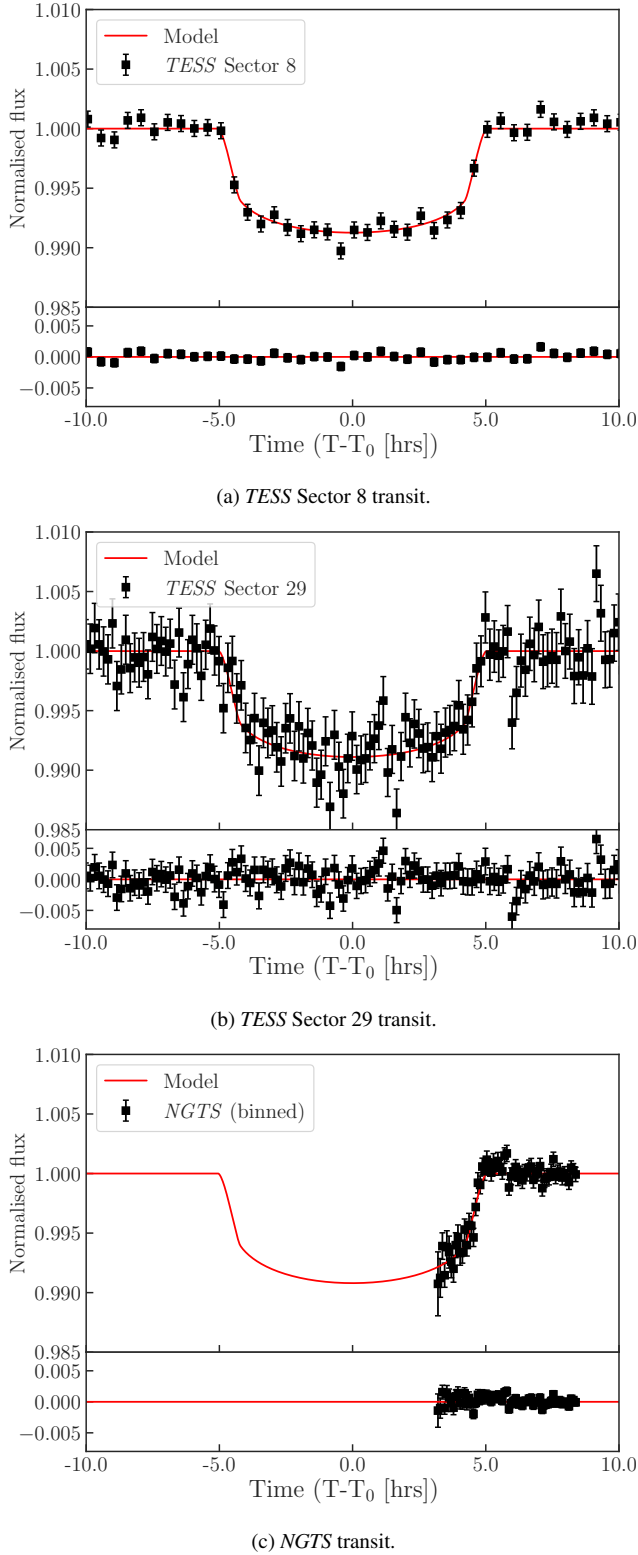


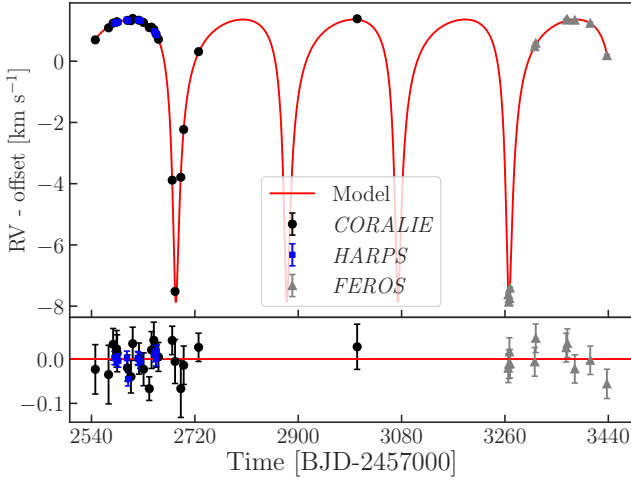
Figure 1. Transit lightcurves of NGTS-EB-7 normalised to the out-of-transit flux levels. Each panel shows the median transit model (see Section 5.1) as a solid red line. The transit data plotted is shown as black square markers with errorbars. The top panel of each subfigure shows the data and model while the lower panel of each shows the residuals after the model has been subtracted from the observed data.

Table 2. Radial velocity measurements of NGTS-EB-7.

Time (BJD-2457000)	Radial Velocity (kms^{-1})	Exposure time (seconds)	SNR*	Airmass
<i>CORALIE</i>				
2546.65717	79.12 ± 0.05	2100	9.4	1.39
2569.71955	79.52 ± 0.06	2100	6.4	1.08
2577.71406	79.67 ± 0.03	2100	11.8	1.08
2583.75381	79.71 ± 0.04	2100	10.2	1.11
2584.70351	79.71 ± 0.04	1800	10.2	1.08
2602.63912	79.76 ± 0.02	2100	15.2	1.08
2608.75240	79.75 ± 0.03	2101	12.1	1.29
2611.73879	79.83 ± 0.03	2101	12.0	1.27
2622.72229	79.77 ± 0.03	2100	13.5	1.31
2630.69521	79.69 ± 0.03	2100	10.4	1.30
2640.60792	79.53 ± 0.02	2100	15.3	1.13
2644.57483	79.54 ± 0.04	2100	9.4	1.10
2648.53875	79.47 ± 0.04	2100	9.2	1.08
2652.57233	79.31 ± 0.02	2100	15.1	1.13
2656.57356	79.14 ± 0.03	2100	13.0	1.15
2680.56890	74.54 ± 0.03	2100	12.7	1.34
2685.51048	70.91 ± 0.05	1500	7.6	1.19
2695.51201	74.64 ± 0.06	1500	5.9	1.28
2700.51825	76.20 ± 0.04	1500	9.6	1.37
2726.46561	78.74 ± 0.03	2100	13.5	1.46
3002.63475	79.81 ± 0.05	1500	8.8	1.17
<i>HARPS</i>				
2579.82769	79.546 ± 0.005	1800	25.1	1.28
2582.76821	79.568 ± 0.004	1800	32.9	1.14
2584.77773	79.589 ± 0.005	1800	25.9	1.17
2586.77178	79.593 ± 0.004	1800	27.8	1.17
2601.71653	79.668 ± 0.007	1800	19.1	1.14
2603.75581	79.625 ± 0.006	1800	22.3	1.25
2620.64952	79.662 ± 0.004	1800	28.5	1.12
2621.67762	79.656 ± 0.005	1800	27.9	1.17
2624.70819	79.636 ± 0.006	1800	24.3	1.29
2625.73369	79.631 ± 0.008	1800	19.1	1.42
2649.65720	79.289 ± 0.005	1800	26.2	1.37
2651.60515	79.237 ± 0.005	1800	26.3	1.20
2652.64649	79.186 ± 0.009	1800	16.1	1.35
2653.57857	79.168 ± 0.005	1800	27.2	1.15
<i>FEROS</i>				
3268.77318	70.787 ± 0.010	1200	50	1.10
3266.74627	70.550 ± 0.009	1200	55	1.19
3267.81058	70.670 ± 0.009	1200	61	1.09
3268.77318	71.009 ± 0.009	1200	61	1.13
3311.81894	78.894 ± 0.010	1200	53	1.24
3313.61205	79.005 ± 0.010	1200	53	1.21
3366.70585	79.764 ± 0.010	1200	50	1.39
3368.64831	79.783 ± 0.010	1200	50	1.20
3381.57640	79.758 ± 0.008	1200	68	1.12
3408.52850	79.657 ± 0.009	1200	58	1.17
3437.50366	78.601 ± 0.012	1200	42	1.33

* For *CORALIE* we list the recorded SNR of spectral order 62, while for *HARPS* we use order 64. The SNR values for *FEROS* are described in § 3.3.

ure 2, and indicates that the eclipsing body is a low-mass star on a highly eccentric orbit.



(a) Radial velocities as a function of time.

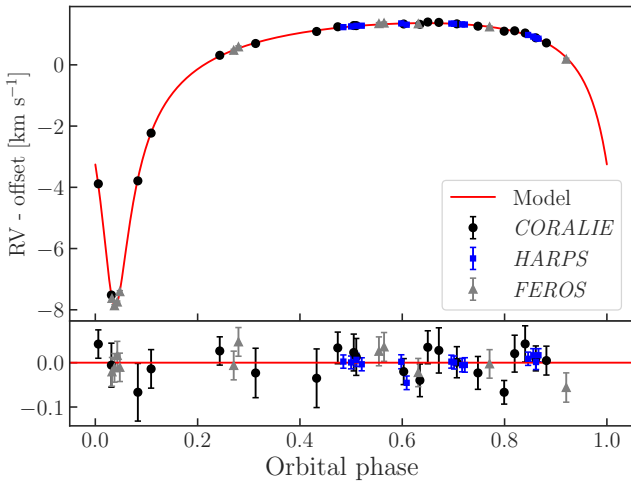

 (b) Radial velocities after phase-folding on the orbital period of 193.35875 ± 0.00034 days.

Figure 2. Radial velocity measurements of NGTS-EB-7. Data points from CORALIE are denoted with a black circle, HARPS is shown with a blue square and FEROS with grey triangles. The median fitted RV model is also overplotted in red. The top panel shows the data while the bottom shows the residuals after subtracting the best model fit. Subfigure (a) shows the data plotted versus time while (b) shows the same data as a function of orbital phase.

3.2 HARPS

We also used the High Accuracy Radial velocity Planet Searcher (HARPS; Mayor et al. 2003) spectrograph mounted on the 3.6-m telescope at ESO La Silla Observatory to make additional radial velocity measurements of NGTS-EB-7. Between the nights of 2021/12/31 and 2022/03/15, 14 spectra were taken of NGTS-EB-7 using HARPS¹. All of these observations used an exposure time of 1800 s, and the airmass ranged from 1.42 to 1.14. The spectra were reduced using DRS 3.0.0 and a G8 mask. The resultant RV measurements are presented in Table 2 and shown in Figure 2.

¹ Based on observations collected at the European Southern Observatory under ESO programme 108.22L8.001

3.3 FEROS

We also made use of the Fiberfed Extended Range Optical Spectrograph (FEROS; Kaufer et al. 1999) mounted on the 2.2-m MPG/ESO telescope at ESO La Silla to take further RV measurements of NGTS-EB-7. These observations were performed in the context of the Warm gIaNs the tESS (WINE) collaboration (Brahm et al. 2019; Schlecker et al. 2020; Hobson et al. 2021; Trifonov et al. 2023; Brahm et al. 2023; Jones et al. 2024). Between the nights of 2023/11/17 and 2024/05/07, 11 spectra were taken with exposure times of 1200 s at airmasses ranging between 1.09 and 1.25 resulting in SNRs ranging between 42 and 68. Note that these SNR values are per resolution element and are based on the order centered on the Magnesium triplet around 5150Å. The spectra were reduced using the ceres pipeline (Brahm et al. 2017), resulting in the RV measurements shown in Table 2 and Figure 2. The RV points taken with FEROS include 4 points clustered around the time of periastron, which proved especially useful in constraining the shape of the RV curve (see Section 5.1).

4 PRIMARY STELLAR ANALYSIS

4.1 Catalogue parameters

Catalogue parameters for NGTS-EB-7 are shown in Table 3. These were taken from the 2 Micron All Sky Survey (2MASS; Skrutskie et al. 2006), Gaia data release 3 (Gaia DR3; Gaia Collaboration et al. 2021), the TESS Input Catalogue v8 (TIC 8; Stassun et al. 2019), the AAVSO Photometric All Sky Survey (APASS; Henden & Munari 2014), the Wide field Infrared Survey Explorer (WISE; Wright et al. 2010) and SkyMapper (Keller et al. 2007) catalogues where specified.

4.2 Spectral fitting

To fit accurate stellar atmospheric parameters for the primary we combined the 14 individual HARPS spectra taken for NGTS-EB-7 into a single spectrum with an SNR value of 85. In addition, we masked out certain regions of the spectra that were affected by systematics due to ghosting on the CCD, these masked regions are listed in Table B1.

We used the PAWS pipeline to analyse the HARPS spectra for NGTS-EB-7 in order to obtain accurate stellar parameters for the primary star. It is described in full in Freckelton et al. (2024), however we summarise its function in the remainder of this section. PAWS is built on the *i*spec package (Blanco-Cuaresma et al. 2014b,a). It uses the line list created for the spectrum package (Gray & Corbally 1994) with some minor additions described in Freckelton et al. (2024), as well as the ATLAS 9 set of model atmospheres (Kurucz 2005) to perform fits to spectra using a combined equivalent widths and synthesis method.

The equivalent widths fitting is done on only the Fe I and Fe II lines utilizing the ARES (Sousa et al. 2015) and WIDTH (Sbordone et al. 2004) software packages and the solar abundances collated by Blanco-Cuaresma (2019). The effective temperature (T_{eff}), surface gravity ($\log g$) and metallicity ($[M/H]$) are estimated using this method and, in turn, are then used to estimate a value of the micro-turbulent velocity (v_{mic}) by applying the Gaia-ESO (GES) relation based on the Gaia-ESO survey UVES data release 1 as described in Blanco-Cuaresma et al. (2014b) and Jofré et al. (2014).

The values of T_{eff} and $\log g$ derived from equivalent widths are then used as priors for the synthesis fitting method while the values of $[M/H]$ and v_{mic} are fixed. The SPECTRUM package (Gray & Corbally

Table 3. NGTS-EB-7 A stellar parameters.

Property	Value	Source
<i>Identifiers</i>		
2MASS ID	J06564704-5204263	2MASS (§4.1)
<i>Gaia</i> Source ID	5504617415848984320	<i>Gaia</i> DR3 (§4.1)
TIC ID	238060327	TIC 8 (§4.1)
<i>Coordinates</i>		
RA	6 ^h 56 ^m 47.04 ^s	<i>Gaia</i> DR3 (§4.1)
DEC	−52°04′26.11″	<i>Gaia</i> DR3 (§4.1)
<i>Proper motion and parallax</i>		
μ_{RA} (mas y ^{−1})	4.279 ± 0.013	<i>Gaia</i> DR3 (§4.1)
μ_{DEC} (mas y ^{−1})	16.980 ± 0.013	<i>Gaia</i> DR3 (§4.1)
Parallax (mas)	2.21 ± 0.01	<i>Gaia</i> DR3 (§4.1)
Radial velocity (km s ^{−1})	78.376 ± 0.005	This work (§6.2)
<i>Galactic Kinematics</i>		
<i>U</i> (km s ^{−1})	−33.05 ± 0.16	This work (§6.2)
<i>V</i> (km s ^{−1})	−62.86 ± 0.02	This work (§6.2)
<i>W</i> (km s ^{−1})	−0.84 ± 0.09	This work (§6.2)
v_{tot} (km s ^{−1})	71.02 ± 0.08	This work (§6.2)
e_{gal}	0.31	This work (§6.2)
J_z (kpc km s ^{−1})	1278	This work (§6.2)
<i>Magnitudes</i>		
V (mag)	12.440 ± 0.026	APASS (§4.1)
B (mag)	13.176 ± 0.024	APASS (§4.1)
u (mag)	14.371 ± 0.024	SkyMapper (§4.1)
g (mag)	12.596 ± 0.019	SkyMapper (§4.1)
r (mag)	12.257 ± 0.030	SkyMapper (§4.1)
i (mag)	12.083 ± 0.010	SkyMapper (§4.1)
z (mag)	12.096 ± 0.020	SkyMapper (§4.1)
G (mag)	12.2787 ± 0.0002	<i>Gaia</i> DR3 (§4.1)
BP (mag)	12.6455 ± 0.0006	<i>Gaia</i> DR3 (§4.1)
RP (mag)	11.7458 ± 0.0004	<i>Gaia</i> DR3 (§4.1)
<i>TESS</i> (mag)	11.806 ± 0.006	TIC 8 (§4.1)
J (mag)	11.172 ± 0.024	2MASS (§4.1)
H (mag)	10.858 ± 0.025	2MASS (§4.1)
K (mag)	10.774 ± 0.024	2MASS (§4.1)
W1 (mag)	10.715 ± 0.022	WISE (§4.1)
W2 (mag)	10.765 ± 0.020	WISE (§4.1)
<i>Fitted Atmospheric Parameters</i>		
T_{eff} (K)	5770 ± 110	PAWS (§4.2)
log <i>g</i> (log (cgs))	4.17 ± 0.15	PAWS (§4.2)
[M/H] (‘dex’)	0.26 ± 0.12	PAWS (§4.2)
log R'_{HK}	−5.12 ± 0.17	This work (§4.5)
$v \sin i_{\star}$ (km s ^{−1})	2.7 ± 0.8	PAWS (§4.2)
v_{mic} (km s ^{−1})	1.42 ± 0.03	PAWS (§4.2)
v_{mac} (km s ^{−1})	3.92	PAWS (§4.2)
<i>Derived parameters</i>		
R_{\star} (R_{\odot})	1.45 ^{+0.07} _{−0.06}	isochrones (§4.3)
M_{\star} (M_{\odot})	1.13 ^{+0.06} _{−0.07}	isochrones (§4.3)
Age (Gyr)	10 ± 1	isochrones (§4.3)

1994) is then used to generate synthetic spectra that are iteratively fit to the observed data. Values of T_{eff} , log *g* and the projected stellar rotational velocity ($v \sin i_{\star}$) are fit for and the macroturbulent velocity (v_{mac}) is calculated using the same GES derived relation used for v_{mic} in the portion of the pipeline that determines the equivalent widths. Six iterations were used, which was determined to be the optimal number by Blanco-Cuaresma et al. (2014b). As is standard for PAWS, a value of 100 K is added in quadrature to the errors in T_{eff} as otherwise the errors reported by *i*spec are more precise than the expected accuracy of the atmospheric models used (see Freckleton et al. 2024, for details).

The fitted parameters are shown in Table 3. These values show a temperature consistent with an early G-type star and enriched metallicity as well as a surface gravity consistent with a star evolving off the main sequence. These values were used as priors in order to determine a mass and radius for the star via isochrone model fitting (see Section 4.3).

4.3 Isochrone fitting

We used the *isochrones* package (Morton 2015) to determine a mass and radius of the primary by fitting MIST isochrones (Dotter 2016; Choi et al. 2016). Following Davis et al. (2024) we used the J, H and K infrared band catalogue photometry points as well as the *Gaia* parallax shown in Table 3 and the PAWS fitted parameters as priors. The resulting parameters are shown in Table 3. The uncertainties were estimated by extracting the 84th and 16th percentiles of the posterior sample. To reflect the inherent systematic uncertainty in evolutionary models, we follow the recommendations of Tayar et al. (2022) and add an additional 4.2% error term in quadrature to the stellar radius. We also add errors in quadrature to the mass, and age values of 0.03 M_{\odot} and 1 Gyr, respectively, found by taking the standard deviation of fitted values from different sets of isochrones using the *kiuhoku* package (Tayar et al. 2022).

Since we already knew the star was in a binary, we fitted both a double and single star model but found the parameters for the secondary were in strong disagreement with those obtained from our global fit of the system (see Section 5.1). This is likely due to the secondary contributing a very small amount of light to the passbands used, meaning *isochrones* cannot obtain accurate secondary stellar parameters from these wide band photometric points. The primary parameters changed very little between these two fits, hence we choose to present the single star fit for simplicity.

4.4 Checking against other sources

In order to provide a check on the parameters derived using PAWS and *isochrones* we compare the values obtained from these methods to those from other sources. We use the *Gaia* DR3 and TICv8 catalogues. We also use values obtained from fitting to the spectral energy density (SED) using the *astroARIADNE* package (Vines & Jenkins 2022). Another set was obtained by matching the target spectrum against a library of spectra using *specmatch-emp* (Yee et al. 2017). We also obtained an additional parameter set by fitting against the spectrum using *species* (Soto & Jenkins 2018). We find reasonable agreement across all these sources apart from the *Gaia* metallicity, which is ~ -0.2 ‘dex’. However, due to the relatively small region of the spectrum sampled by *Gaia*, this is likely a systematic effect. This leads us to conclude the values from PAWS and *isochrones* are accurate and we adopt these values for the primary going forward.

4.5 Stellar activity and rotation

A visual inspection quickly shows the out-of-transit *TESS* and *NGTS* lightcurves (see Section 2) to be flat and a Lomb-Scargle periodogram created using `lightkurve` (Lightkurve Collaboration et al. 2018) also returned no significant peaks.

We also calculated $\log R'_{\text{HK}}$ (following the procedure set out in Lovis et al. 2011; Costes et al. 2021) using the coadded *HARPS* spectrum as the individual spectra had insufficient SNR. First we measured the flux at two pass bands centred on the Ca II H and K line cores. The *H* band is centred at 3968.47 Å whilst the *K* band is centred at 3933.664 Å and both have a triangular shape and a Full Width Half Maximum (FWHM) of 1.09 Å. We then measured the flux of two continuum passbands with widths of 20 Å centred at 4001.070 Å (*R*) and 3901.070 Å (*V*). These passband fluxes were then used to calculate the Mt Wilson *S* index using the following equation:

$$S = 1.111 \times \frac{H + K}{R + V} + 0.0153. \quad (1)$$

The multiplication coefficient of 1.111 and additive constant of 0.0153 are calibration terms from Lovis et al. (2011) that map the flux ratios calculated from *HARPS* spectra to the Mt Wilson *S* index. We then use this value to calculate R'_{HK} as described in Noyes et al. (1984):

$$R'_{\text{HK}} = 1.340 \times 10^{-4} \times C_{\text{cf}}(B - V) \times S \times R_{\text{phot}}(B - V), \quad (2)$$

where $C_{\text{cf}}(B - V)$ and $R_{\text{phot}}(B - V)$ are both correction factors based on the photometric *B - V* colour calculated from magnitudes shown in Table 3 that account for varying flux in continuum passbands and the photospheric contribution in the *H* and *K* passbands, respectively. We find a value of $\log R'_{\text{HK}} = -5.12 \pm 0.17$.

In addition, we used equation 3 and 4 from Noyes et al. (1984) to estimate the rotation period of *NGTS-EB-7 B* from $\log R'_{\text{HK}}$ and *B - V*, finding a value of 39 ± 6 d. When we compare this to the upper limit on the rotational period as determined from the stellar radius (R_A) and projected equatorial rotation velocity ($v \sin i_\star$) using equation 1 from Watson et al. (2010) of $P_{\text{rot}} \sin i_\star = 28 \pm 8$ d, we find these values are in reasonable agreement. However, we note that this relation between $\log R'_{\text{HK}}$ and rotational period (and others e.g; Mamajek & Hillenbrand 2008; Stanford-Moore et al. 2020) is calibrated for main sequence stars and may not give an accurate rotation rate for a star evolving off the main sequence. For a simple sanity check on $\log R'_{\text{HK}}$, however, the Noyes et al. (1984) relation is adequate.

In conclusion, a $\log R'_{\text{HK}} = -5.12 \pm 0.17$ strongly suggests that *NGTS-EB-7 A* is a low-activity star. This, along with its relatively slow rotation period, provides additional evidence towards its nature as an old subgiant evolving off the main sequence since older stars are expected to spin-down via magnetic braking (Kraft 1967, 1970), reducing their rotation rate and level of magnetic activity (see figure 6 in Jenkins et al. 2011).

5 ORBITAL SOLUTION

5.1 Global modelling with `allesfitter`

We used the `allesfitter` (Günther & Daylan 2021, 2019) package for Python to simultaneously fit the photometric transit data

and spectroscopic radial velocity data for *NGTS-EB-7* (see section 2 and section 3). `allesfitter` combines other Python packages including `ellc` (Maxted 2016) for modelling light-curves, `emcee` (Foreman-Mackey et al. 2013) for Monte-Carlo Markov-Chain (MCMC) sampling, `dynesty` (Speagle 2020) for nested sampling (Skilling 2004; Skilling 2006) and `celerite` (Foreman-Mackey et al. 2017) for Gaussian processes, among others.

We used a nested sampling approach (Skilling 2004; Skilling 2006) to fit a global model to *NGTS-EB-7*. The photometric solution for the orbital period was ≈ 193 days and the RV periodogram also returned a peak with a false alarm probability $< 1\%$ at this value. Hence, we set a uniform prior on the orbital period (*P*) between 192 and 194 days. Additionally, a fit was carried out on just the *TESS* Sector 8 data to obtain priors on the epoch ($T_{0,B}$), radius ratio (R_B/R_A), semi-major axis ($(R_A + R_B)/a$) and orbital inclination ($\cos i_B$) of the system. The eccentricity and argument of periastron of the system were parameterised as the terms $\sqrt{e} \cos \omega$ and $\sqrt{e} \sin \omega$ and fitted each with uniform priors between -1 and 1 . Similarly we fit the inclination of the system ($\cos i$) using a uniform prior between 0 and 1 . We used a quadratic limb darkening model described in Kipping (2013) and used the Limb Darkening ToolKit (`ldtk`; Parviainen & Aigrain 2015) package to determine priors on the limb darkening coefficients (q_1 and q_2 , for each instrument) based on the observing filters and primary star properties.

To fit the out-of-transit variability for the *TESS* lightcurves (see Section 2.1) we used Gaussian processes (GPs) with a Matern 3/2 kernel. There was not sufficient out-of-transit data available for the night of the *NGTS* egress observation to use a GP so we did not model out-of transit variation for the *NGTS* data (see Section 2.2), however we found the variability out of transit for these data was sufficiently low to justify this approach. However, we did include an additional error term ($\log \sigma$) for *NGTS* assuming white noise. Priors on the GP terms ($\ln \sigma$ and $\ln \rho$) and the additional error term ($\log \sigma$) for each *TESS* sector were obtained by using the `estimate_noise_out_of_transit` function included in the `allesfitter` package to perform an MCMC fit with 100 walkers, 2000 burn steps and 3000 total steps to fit these parameters to the out of transit data. This same method was also used to obtain a prior on the error term for *NGTS*. In addition, we included jitter terms ($\log \sigma$) for *HARPS*, *CORALIE* and *FEROS* in the fit. We also fitted for a radial velocity baseline/offset term for each instrument using the *Gaia* DR3 measured radial velocity of the system as a prior (see Table 3). The combined RV data plotted in Figure 2 was produced by subtracting the fitted baseline term for each instrument (which are reported in Table A1) from the data.. For the semi-amplitude (*K*) we set a uniform prior between 0 and 12 km s^{-1} .

It should be noted that we do not include a surface brightness ratio parameter in our global model fit due to the considerably lower flux contribution from the secondary. Using a maximum estimate of the flux ratio in the *TESS* band (see Section 6.3.3) we find that the contribution of the secondary to the total binary flux is less than 0.05% . The dilution effect from the secondary flux is thus only able to affect our derived secondary radius by at most $\sim 0.22\%$, which is over an order of magnitude smaller than the statistical uncertainty on the radius that we ultimately obtain (see Table 4).

The transit and RV data is shown with the fitted models in Figures 1 and 2, respectively, while a selection of parameters fitted from the global model can be found in Table 4. The full set of parameters outputted by `allesfitter` can be found in Appendix A with fitted parameters and their priors shown in Table A1 and derived parameters in Tables A2 and A3. In addition the default `allesfitter` corner plots are shown in Appendix C.

5.2 Modified Mass function

We follow the method described in [Davis et al. \(2024\)](#) to semi-empirically determine the masses of the primary and secondary, with only the radius of the primary (R_A) being model dependent and every other parameter being either a constant or an observable we can fit for as described in Section 5.1. We perform all of the calculations in this section using the full posterior sample from `allesfitter` for the observables and from `isochrones` for R_A . The observables used in these equations are not directly fitted by `allesfitter` except for the orbital period, P , but can be calculated entirely using `allesfitter` observables as shown below:

$$\frac{a}{R_A} = \frac{1 + (R_B/R_A)}{(R_A + R_B)/a} \quad (3)$$

$$e = (\sqrt{e} \sin \omega)^2 + (\sqrt{e} \cos \omega)^2 \quad (4)$$

$$\sin i = \sqrt{1 - (\cos i)^2} \quad (5)$$

To begin deriving the parameters, we take the primary star density as defined by Kepler's law:

$$\frac{M_A}{R_A^3} = \frac{4\pi^2}{G P^2} \left(\frac{a}{R_A} \right)^3 - \frac{M_B}{R_A^3}, \quad (6)$$

where G is the gravitational constant, a is the orbital semi-major axis, P the orbital period and M_A , M_B , R_A and R_B are the masses and radii of the primary and secondary, respectively. We can then rearrange Equation 6 for the total mass of the binary:

$$M = M_A + M_B = \frac{4\pi^2}{G P^2} \left(\frac{a}{R_A} \right)^3 R_A^3. \quad (7)$$

For *NGTS-EB-7 AB*, we find a total mass of $M = 1.14^{+0.06}_{-0.08} M_\odot$. We then calculate the modified mass function f_m . We refer to this mass function as 'modified' since it contains a $\sin^3 i$ term, which is absent from the typical spectroscopic mass function since the inclination is nearly impossible to determine from spectroscopic observations alone. However, since *NGTS-EB-7 AB* is eclipsing, we can include this term as shown in the equation taken from [Hilditch \(2001\)](#) below:

$$f_m = \frac{(1 - e^3)^{3/2}}{\sin^3 i} \frac{PK^3}{2\pi G}. \quad (8)$$

From this, we determine a value of $f_m = 0.0000675 \pm 0.000005 M_\odot$. This mass function can also be expressed as:

$$f_m = \frac{M_B^3}{(M_A + M_B)^2}, \quad (9)$$

which can be substituted into Equation 7 and solved for the primary and secondary mass:

$$M_B = \sqrt[3]{f_m M^2}, \quad (10)$$

for which we obtain a value of $M_B = 0.096 \pm 0.002 M_\odot$ and $M_A = M - M_B = 1.05^{+0.06}_{-0.07} M_\odot$. Our value of M_B obtained using this method is smaller than that obtained from `isochrones` by $0.08 M_\odot$. However, the difference between both values is only slightly $> 1\sigma$ and thus is unlikely to be significant.

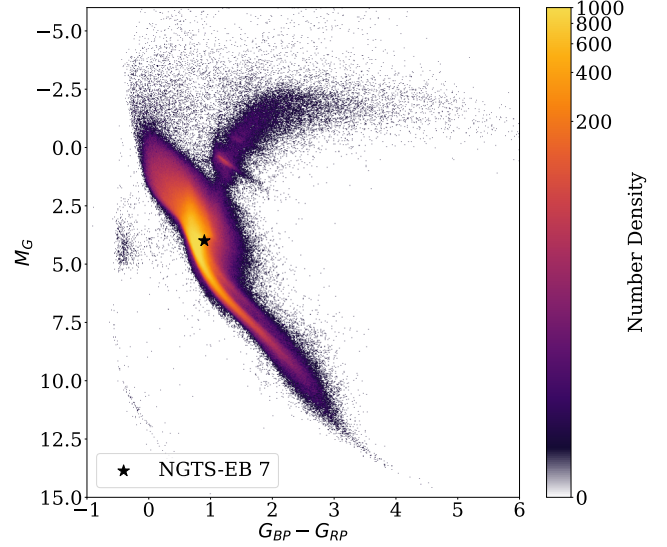


Figure 3. *Gaia* DR3 Hertzsprung Russell diagram with the position of *NGTS-EB-7 A* highlighted with a black star symbol. *Gaia* BP-RP colour is plotted against absolute magnitude in the G band for all stars in the crossmatched SPOC FFI sample described in [Doyle et al. \(2024\)](#). The position of *NGTS-EB-7 A* shown is consistent with a star beginning to move off the main sequence.

6 RESULTS AND DISCUSSION

6.1 The *NGTS-EB-7 AB* system

We find *NGTS-EB-7 A* is likely a metal rich ($[M/H]=0.26 \pm 0.12 \text{ dex}$) evolved early G-type star, with an effective temperature of $5770 \pm 110 \text{ K}$. The enhanced metallicity of the primary is somewhat unusual and falls towards the upper end of what is expected for binary systems (see figure 9 in; [Jenkins et al. 2015](#)). The evolved nature of the primary is apparent from the low value of $\log g=4.17 \pm 0.15$ that we measured from its spectra as well as its position on a Hertzsprung Russell (HR) diagram (see Figure 3). We find a radius of $1.45^{+0.07}_{-0.06} R_\odot$ and a mass of $1.13^{+0.06}_{-0.07} M_\odot$. The evolved nature of the primary also allows us to strongly constrain its age to $10 \pm 1 \text{ Gyrs}$.

For the secondary stellar companion, our orbital solution from fitting a global model (see Section 5.1) finds a mass of $0.096^{+0.003}_{-0.004} M_\odot$ ($102^{+4}_{-5} M_J$) and a radius of $0.125 \pm 0.006 R_\odot$. As can be seen in Figure 4a, this places *NGTS-EB-7 B* as a late M dwarf, similar in size to *TRAPPIST-1* ([Gillon et al. 2017](#)) and close to the hydrogen burning limit ($\approx 80 M_J$; [Chabrier et al. 2023](#)) and the boundary between main sequence stars and brown dwarfs.

In addition, we find the secondary companion is on a highly eccentric orbit ($e=0.71436 \pm 0.00085$), which is plotted in Figure 5, and a long period of $193.35875 \pm 0.00034 \text{ days}$. The eccentricity of the companion's orbit, along with its mass, is consistent with the stellar regime described in [Bowler et al. \(2020\)](#) who found that high mass brown dwarfs and stellar companions show generally higher orbital eccentricities than low-mass brown dwarfs or planets – showing a difference in formation mechanism. Since *NGTS-EB-7 B* belongs to the stellar regime it is unlikely that it formed in a protoplanetary disk like a planet or low-mass brown dwarf. As Figures 4b and 4c show, *NGTS-EB-7 B* has one of the longest-period and most eccentric orbits of any low mass eclipsing binary companions known. The closest orbital separation of the binary is wide enough (at $0.189 \pm 0.009 \text{ AU}$) that we can expect that the evolution of *NGTS-EB-7 B* is similar to that of a single star in a similar mass and radius range, with little

Table 4. NGTS-EB-7 B parameters.

Parameter	Value	Source
<i>Fitted parameters</i>		
R_B/R_A	$0.0869^{+0.0012}_{-0.0011}$	allesfitter (§5.1)
$(R_A + R_B) / a$	$0.01098^{+0.00026}_{-0.00016}$	allesfitter (§5.1)
$\cos i$	$0.0032^{+0.0028}_{-0.0021}$	allesfitter (§5.1)
$T_{0;\text{tra}}$ (BJD)	$2459486.0746^{+0.0016}_{-0.0015}$	allesfitter (§5.1)
P_{orb} (days)	193.35875 ± 0.00034	allesfitter (§5.1)
$\sqrt{e} \cos \omega$	-0.83371 ± 0.00076	allesfitter (§5.1)
$\sqrt{e} \sin \omega$	0.1389 ± 0.0028	allesfitter (§5.1)
K (km s^{-1})	4.6150 ± 0.0096	allesfitter (§5.1)
<i>Derived parameters</i>		
$R_B(R_J)$	1.219 ± 0.058	allesfitter (§5.1)
$R_B(R_\odot)$	0.125 ± 0.006	allesfitter (§5.1)
$M_B(M_J)$	102^{+4}_{-5}	This work (§5.2)
$M_B(M_\odot)$	$0.096^{+0.003}_{-0.004}$	This work (§5.2)
$\log g$ (\log (cgs))	5.22 ± 0.03	This work (§6.3)
a (AU)	0.661 ± 0.033	allesfitter (§5.1)
r_{apastron} (AU)	1.13 ± 0.06	This work*
$r_{\text{periastron}}$ (AU)	0.189 ± 0.009	This work*
b_{tra}	$0.138^{+0.12}_{-0.090}$	allesfitter (§5.1)
b_{occ}	$0.12^{+0.09}_{-0.08}$	This work (§6.3.1)
i (deg)	$89.82^{+0.12}_{-0.16}$	allesfitter (§5.1)
e	0.71436 ± 0.00085	allesfitter (§5.1)
ω (deg)	$170.54^{+0.20}_{-0.19}$	allesfitter (§5.1)
T_{14} (hrs)	$10.06^{+0.11}_{-0.10}$	(§5.1)
T_{23} (hrs)	$8.406^{+0.092}_{-0.099}$	(§5.1)
T_{58} (hrs)	12.7 ± 0.2	This work (§6.3.2)
T_{67} (hrs)	10.6 ± 0.2	This work (§6.3.2)
$T_{0;\text{occ}}$ (BJD)	2459503.5 ± 0.1	This work (§6.3.2)
$\phi_{0;\text{occ}}$	0.0900 ± 0.0006	This work (§6.3.2)

* The values $r_{\text{apastron}} = a(1 + e)$ and $r_{\text{periastron}} = a(1 - e)$ were calculated from the eccentricity, e , and semi-major axis, a , values returned from *allesfitter*.

effect from interaction with the primary star. This makes this system useful to test potential radius inflation mechanisms proposed for late M dwarf companions, this is discussed further in Section 6.5.

6.2 Galactic kinematics and population membership

We computed (U, V, W) galactic velocities using an updated version of the method from Johnson & Soderblom (1987). To do this, we used the parallax and proper motion values from *Gaia* DR3 (see Table 3) and calculated an error weighted mean of the instrumental radial velocity baselines shown in Table A1. This value is also shown in Table 3 and is in reasonable agreement with the *Gaia* DR3 value. We also computed the Galactic total velocity, eccentricity and angular momentum of the orbit Z-component. The resulting values are all shown in Table 3.

We used the velocities from Table 3 to determine the probability of membership for the thin disk, thick disk and halo using the framework from Bensby et al. (2003) and the Galactic standard velocity dispersions from Bensby et al. (2003, 2014); Reddy et al. (2006); Chen et al. (2021). We also corrected for the local standard of rest (LSR) using the values from Almeida-Fernandes & Rocha-Pinto (2018). Lastly we combined the thin disk, thick disk and halo probabilities from

the different velocity dispersions using a Bayesian Model Averaging method to calculate population membership probabilities.

The Bayesian analysis returned a probability of 80% for thin disk membership, 20% for thick disk and 0% for the Galactic halo. While this indicates the star is likely a thin disk member, the above average total velocity (v_{tot}), eccentricity (e_{gal}) and angular momentum (J_z) shown in Table 3 would usually imply a thick disk or halo star (Yan et al. 2019). We conclude that the most likely scenario is that NGTS-EB-7 is a thin disk system that has undergone some kinematic heating in the recent past; perhaps through gravitational interactions with other stars.

Rossiter-McLaughlin (RM; Rossiter 1924; McLaughlin 1924; Triaud 2018) measurements could be used to constrain the spin-orbit obliquity of the companion star, providing further clues to the dynamical history of the system and potential previous encounters with other stars. Using equation 1 from Triaud (2018), we estimate an RM amplitude of $\sim 20 \text{ m s}^{-1}$, which is detectable by current generation RV instruments such as *HARPS* (Mayor et al. 2003).

6.3 Secondary eclipse

Detection of a secondary eclipse / occultation of NGTS-EB-7 B by the primary would allow for a more robust estimation of its luminosity and therefore temperature. Given the discrepancy between measured M dwarf temperatures and those predicted by models (Spada et al. 2013; Parsons et al. 2018), temperature measurements of detached late M dwarf companions such as NGTS-EB-7 B via secondary eclipse or other means is vital to understanding this class of star as a whole.

6.3.1 Inclination

To determine if the system is inclined such that a secondary eclipse could occur we calculated the impact parameter at occultation b_{occ} using the formula laid out in Winn (2014). Using a Monte-Carlo approach to estimate errors we find $b_{\text{occ}} = 0.12^{+0.09}_{-0.08}$, and hence we predict that a secondary eclipse of NGTS-EB-7 B should be detectable with sufficient photometric precision.

6.3.2 Timing

We used the `contact_points` function from the `pycheops` package (Maxted et al. 2022) in order to calculate the predicted times of contact points during secondary eclipse t_5, t_6, t_7 and t_8 using the values fitted from our orbital solution (see Section 5.1 and Table 4). We then used these to calculate the mid eclipse time ($T_{0;\text{occ}} = 2459503.5 \pm 0.1$ BJD), which corresponds to phase $\phi_{0;\text{occ}} = 0.0900 \pm 0.0006$. This would put a secondary eclipse in Sector 8 of the TESS data alongside the primary transit (although it cannot be seen in the data). We also calculate the full and total durations of occultation ($T_{\text{tot};\text{occ}} = T_{58} = 12.7 \pm 0.2$ hrs, $T_{\text{full};\text{occ}} = T_{57} = 10.6 \pm 0.2$ hrs,). The uncertainties were estimated via a monte-carlo approach and we quote the mean and standard deviation of our samples as the value and uncertainty for each parameter.

6.3.3 Estimated depth and detectability

We did not detect a secondary eclipse in any of the lightcurves obtained for NGTS-EB-7. A visual inspection of the lightcurves did not yield any detections and attempting to fit a secondary eclipse with *allesfitter* also returned a depth of 0. Since the inclination

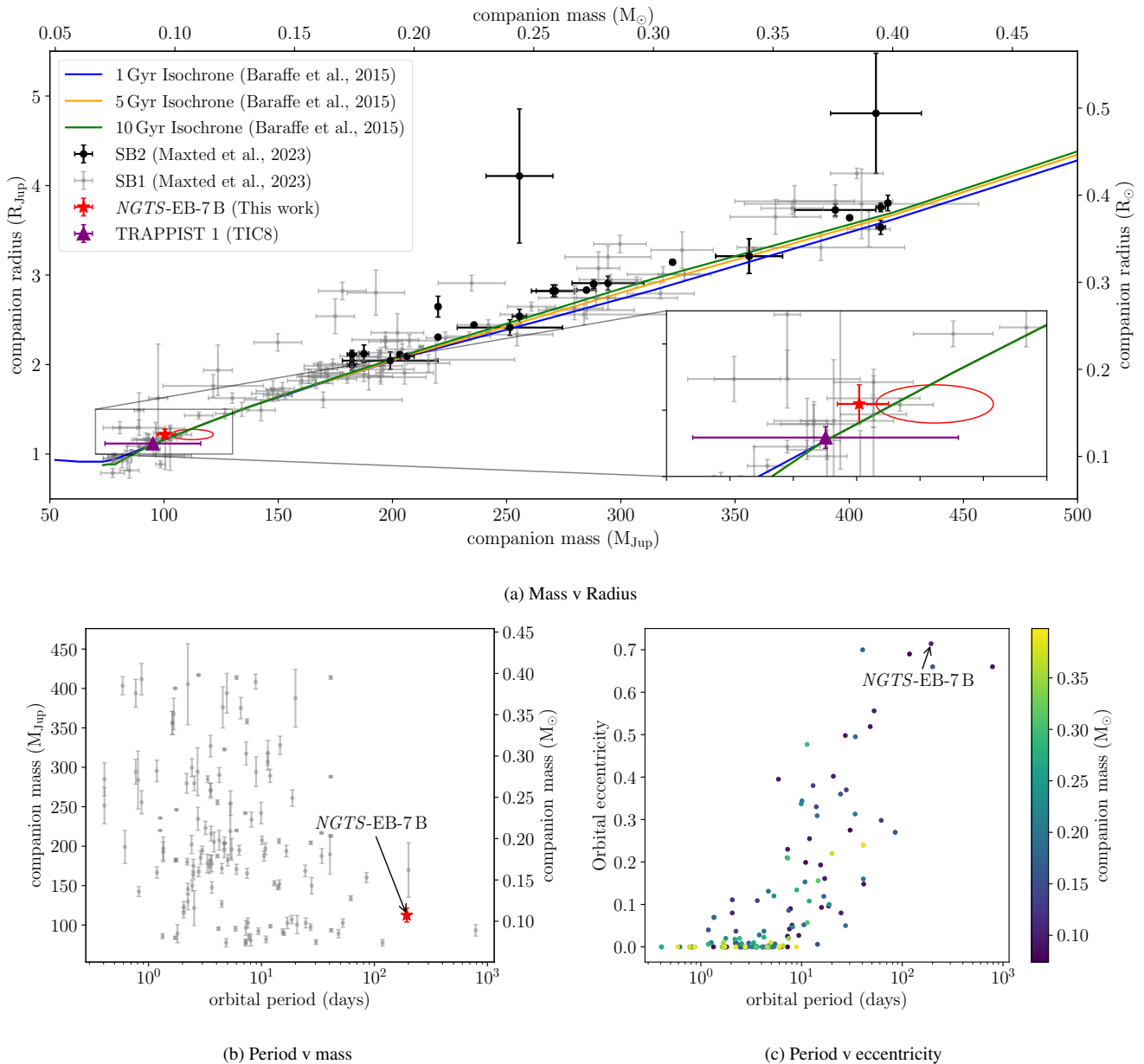


Figure 4. Plots of the low-mass companions of eclipsing binaries as taken from the catalogue of [Maxted et al. \(2023\)](#) which contains all systems from the EBLM project and other systems with a quoted precision of 5% or less. *NGTS-EB-7 B* is shown as a red star for comparison. **Top (a):** Mass radius plot of EBLM companions. Single lined binaries (SB1) are shown by grey dot markers while double lined binaries (SB2) are shown with black circle markers. In addition to the red star with errorbars representing the mass and radius of *NGTS-EB-7 B* as calculated in Section 5.2, the uncorrected values from *allesfitter* are shown with a red ellipse (note that both are within $1-\sigma$ agreement – see Section 6.5). *TRAPPIST-1* is also plotted as a purple triangle for comparison. Also shown is the 1, 5 and 10 Gyr isochrones from [Baraffe et al. \(2015\)](#) plotted as blue, orange and green solid lines, respectively. An inset axis is shown zoomed in around *NGTS-EB-7 B*. **Bottom left (b):** Orbital period plotted on a logarithmic scale against companion mass. **Bottom right (c):** Orbital period plotted on a logarithmic scale against orbital eccentricity and coloured by mass. Note that the error in eccentricity is too small to be seen.

of the system is such that a secondary eclipse should occur this is most likely due to insufficient photometric precision. To test this we begun by estimating secondary eclipse depths of *NGTS-EB-7 B* in various photometric bandpasses.

We chose to test temperatures of the secondary between 2450K and 3050K as quoted for the M9V and M5V spectral types in [Pecaut & Mamajek \(2013\)](#), which is the range we expect *NGTS-EB-7 B* to

lie in. We then used the *expecto*² package to fetch PHOENIX model spectra ([Husser et al. 2013](#)) for the primary and secondary based on the respective values of T_{eff} and $\log g$. The value of $\log g$ for the secondary was calculated using the relation from [Smalley \(2005\)](#) finding a value of $5.22 \pm 0.03 \log(\text{cgs})$ We then use these model

² Available at: <https://github.com/bmorris3/expecto>

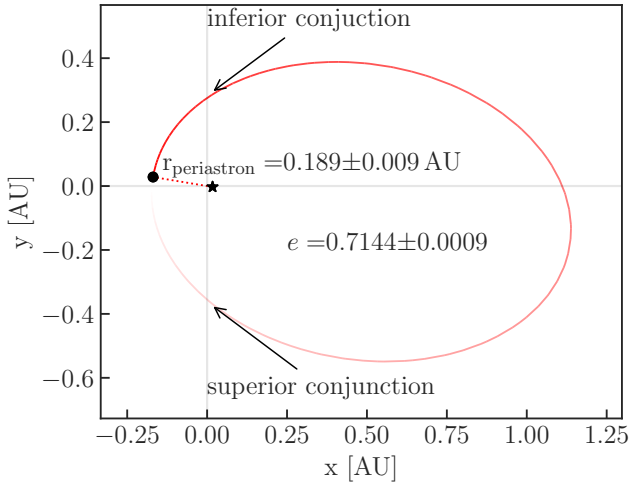


Figure 5. Face down orbital view of the *NGTS-EB-7* AB system generated with *rebound* (Rein & Liu 2012; Rein & Spiegel 2015). The plot coordinates are centered on the centre of mass of the system. The primary is as shown with a black star symbol and the secondary is shown as a black circle and its orbital path is visible as a red ellipse. The periastron of the orbit is denoted with a red dashed line. The inferior conjunction (transit) and superior conjunction (secondary eclipse) are both labelled with black arrows.

Table 5. Estimated secondary eclipse depths for *NGTS-EB-7* B.

Bandpass	Depth (ppm)
<i>TESS</i>	108-370
<i>NGTS</i>	32-174
<i>CHEOPS</i>	60-224
<i>PLATO</i>	71-238
J	539-1153
H	685-1459
K	923-1879

spectra along with various transmission filters and the fitted radius ratio to calculate the possible depth ranges shown in Table 5.

The depths we find for *TESS* and *NGTS* are similar to the noise profiles for both instruments, which explains the non-detection of any secondary eclipse we see in all the photometric data for the target (see Section 2). We do, however, find significantly greater depths for the 2MASS J, H and K bandpasses indicating the eclipse would be detectable with these filters - although observing sufficient baseline to measure the depth accurately and precisely may be difficult from the ground given the expected long duration of eclipse. In addition we expect similar depths for *CHEOPS* and *PLATO*, while both of these are similar depths as predicted for *TESS* and *NGTS*, the greater precision of *CHEOPS* and *PLATO* may allow them to detect the secondary eclipse where *TESS* or *NGTS* may not be able to. *NGTS-EB-7* is in the P5 sample of the *PLATO* (Rauer et al. 2014) Input Catalogue (PIC; Montalto et al. 2021) and is situated near the centre of the *PLATO* LOPS2 field and is hence observable with 24 cameras (Montalto et al. 2021; Eschen et al. 2024). This is shown in Figure 6. The predicted noise is recorded in the *PLATO* Input Catalogue as calculated using the *PLATO* Instrument Noise Estimator (PINE; Börner et al. 2024). Observing *NGTS-EB-7* with 24 *PLATO* cameras is predicted to result in a precision of 101.8 ppm in one hour. This gives strong prospects of the secondary eclipse being detectable by *PLATO*. With *PLATO*'s long baseline of at least two years (possibly

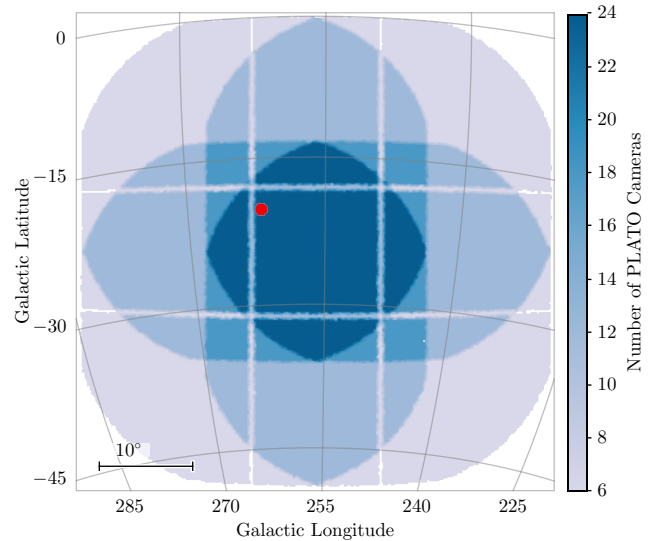


Figure 6. The *PLATO* LOPS2 field. Different shades of blue represent the areas where a star is observed with either 6, 12, 18 or 24 cameras, with darker shades indicating a greater number of cameras. *NGTS-EB-7* (marked with a red dot) is located in the dark blue region in the centre which will be observed with 24 cameras.

4) in LOPS2, 3-4 transits and/or secondary eclipses should be visible, allowing a building up of SNR with additional detections.

6.4 Tidal circularisation

Tidal effects between binaries at large orbital separations such as *NGTS-EB-7* are expected to be extremely weak. We use the semi-empirical relations from Claret & Cunha (1997) to estimate the tidal circularisation timescale of the system. We also estimate the timescale using the formulae laid out in Jackson et al. (2008). These formulae do assume that the rotation of the primary and secondary stars is not synchronised, the eccentricity of the system is low and the orbital period is below 10 days. Whilst the latter two assumptions are certainly not true for *NGTS-EB-7* AB, this can still provide a useful order of magnitude estimate and sanity check for the values estimated using the Claret & Cunha (1997) method. From the Claret & Cunha (1997) relation we find the circularisation timescale should be on the order of 10^6 Gyr while the Jackson et al. (2008) relation returns values between $10^4 - 10^6$ Gyr depending on the chosen tidal quality factors. Both of these estimates are several orders of magnitude longer than the age of the universe, which leads us to conclude that the system will not circularise before the primary enters its red giant phase - at such time the system will likely become a common-envelope system. As well as the tidal circularization timescale, we also estimate the tidal synchronisation timescale using equation 14 from Maxted et al. (2023), finding a value of $\sim 10^5 - 10^6$ Gyr depending on rotational period. Again these lead us to conclude that tidal interactions in the system are incredibly weak and that no meaningful interaction between the primary and secondary will occur until the system reaches the common envelope stage.

6.5 Radius inflation

Many models attempting to explain the ‘radius-inflation’ problem for M-dwarfs rely on magnetic effects (e.g; Chabrier et al. 2007;

López-Morales 2007; Morales et al. 2022). According to these models the inflation should be more prevalent in close binaries where interactions with the primary will ‘spin up’ the secondary and lead to an enhanced magnetic dynamo. This faster rotation and coupled magnetic effects can inflate the radius of the secondary. However, it is currently unclear whether radius inflation is limited to only short-period EBLMs. von Boetticher et al. (2019) found no link between orbital period and radius inflation while Swayne et al. (2024) found inflation was greater for M dwarfs in short-period binaries. However, these studies were each based on a relatively small number of EBLM systems, all with considerably shorter orbital periods than *NGTS-EB-7 B*. Given its position in the extreme long-period region of parameter space shown in Figures 4b and 4c, the potential inflation of *NGTS-EB-7 B* has strong ramifications to these magnetic models attempting to explain inflation.

NGTS-EB-7 B appears to have a radius $\sim 1.0\%$ above what the nearest point on the isochrone models from Baraffe et al. (2015) would predict (see Figure 4a). This is consistent with Maxted et al. (2023) who conclude that radius inflation for the lowest-mass M-dwarfs is $\sim 2\%$. However, we find this difference to be statistically insignificant as the vector difference between the mass and radius of *NGTS-EB-7 B* and the nearest point of the isochrone is 0.97σ . While more precise mass and radius measurements could increase this, given the already relatively precise mass and radius of *NGTS-EB-7 B*, we find it highly unlikely that this discrepancy is statistically significant and thus is unlikely to be astrophysical in nature. It should also be noted that the inflation is model dependent, and comparing the mass and radius of *NGTS-EB-7 B* to another evolutionary model with different input physics (e.g. the equation of state) will change the apparent inflation. Filling out the long-period parameter space could allow for a population level determination of radius inflation as a function of orbital period, but this is currently difficult while the number of extremely long-period systems remains low.

7 SUMMARY AND CONCLUSION

The *NGTS-EB-7 AB* system is a long-period and highly eccentric EBLM system with an evolved G-type primary and late M-dwarf secondary near the hydrogen burning limit. We expect tidal effects on both the primary and secondary to be negligible due to the relatively wide orbital separation of both stars at periastron, despite the high eccentricity.

We first discovered evidence of a secondary companion via a single transit detection in *TESS* Sector 8 with a depth consistent with a Jupiter-sized planet and an additional transit in Sector 29 which we extracted from the data despite initially being hidden due to scattered Earth light. We then began a campaign of spectroscopic and photometric follow-up observations. An observation of a transit egress with *NGTS* was able to confirm the orbital period as 193.35875 ± 0.00034 days. Radial velocity measurements from *CORALIE* and *HARPS* spectra revealed the companion was stellar in mass and on a highly eccentric orbit. The spectra used to measure these radial velocities were also used to measure atmospheric parameters of the primary star *NGTS-EB-7 A*, revealing it to be an evolved G sub-giant.

Global analysis of the photometric and radial velocity data provided a complete orbital solution for the system with an orbital period as 193.35875 ± 0.00034 days and an eccentricity of 0.71436 ± 0.00085 , making *NGTS-EB-7 AB* one of the longest period and most eccentric EBLMs known. This allowed us to measure a mass of $102^{+4}_{-5} M_J$ and a radius of $1.219 \pm 0.058 R_J$, which is near

the hydrogen limit ($\sim 80 M_J$). We compared this against evolutionary models from the literature and found a difference of 1.26σ for the radius, which indicates *NGTS-EB-7 B* is unlikely to be inflated. More precise mass and radius measurements could refine this difference and potentially find a significant deviation but this is unlikely.

Longer-period M dwarf secondary companions are further away from their primaries allowing their evolution to be reasonably approximated as analogous to single star evolution for a similar spectral type, which makes them useful for calibrating evolutionary models for single M dwarfs. The *NGTS-EB-7 AB* system provides a valuable benchmark for comparison against such models, with well constrained parameters including stellar age due to the evolved nature of the primary. Further RV measurements, focused around periastron, could further constrain the mass of *NGTS-EB-7 B*, allowing for an accurate determination of whether its radius is inflated. In addition, *NGTS-EB-7* is located near the centre of the proposed southern LOPS2 field for the upcoming *PLATO* mission (Rauer et al. 2014). With the longer observation baseline and greater photometric precision of *PLATO* it would be possible to detect additional transits of *NGTS-EB-7 B* and further refine its radius as well as detecting its secondary eclipse and potentially even rotational modulation of *NGTS-EB-7 A*.

As the *TESS* mission progresses and additional observatories with longer observation baselines such as *PLATO* become available, more discoveries of bright nearby long-period EBLMs will become possible. This will allow the region of parameter space currently occupied by *NGTS-EB-7 B* and a few other systems to become more populated - allowing for population level analysis of M-dwarf inflation at these long-period regimes.

ACKNOWLEDGEMENTS

We would like to thank the assistant editor and anonymous reviewer for their comments that helped to improve this paper.

This paper includes data collected by the *TESS* mission. Funding for the *TESS* mission is provided by the NASA Explorer Program. Resources supporting this work were provided by the NASA High-End Computing (HEC) Program through the NASA Advanced Supercomputing (NAS) Division at Ames Research Center for the production of the SPOC data products. The *TESS* team shall assure that the masses of fifty (50) planets with radii less than $4R_{\oplus}$ are determined.

We acknowledge the use of public *TESS* Alert data from pipelines at the *TESS* Science Office and at the *TESS* Science Processing Operations Center.

This paper includes data collected by the *TESS* mission that are publicly available from the Mikulski Archive for Space Telescopes (MAST).

This work is based in part on data collected under the *NGTS* project at the ESO La Silla Paranal Observatory. The *NGTS* facility is operated by a consortium of institutes with support from the UK Science and Technology Facilities Council (STFC) under projects ST/M001962/1, ST/S002642/1 and ST/W003163/1.

TR is supported by an STFC studentship. C.A.W. and E.dM. would like to acknowledge support from the UK Science and Technology Facilities Council (STFC, grant number ST/X00094X/1). JSJ gratefully acknowledges support by FONDECYT grant 1240738 and from the ANID BASAL project FB210003. This work has been carried out within the framework of the NCCR PlanetS supported by the Swiss National Science Foundation under grants 51NF40_182901 and 51NF40_205606. EG gratefully acknowledges support from the

UK Science and Technology Facilities Council (STFC; project reference ST/W001047/1).

R.B. acknowledges support from FONDECYT Project 1241963 and from ANID – Millennium Science Initiative – ICN12_009.

For the purpose of open access, the author has applied a Creative Commons Attribution (CC BY) licence to the Author Accepted Manuscript version arising from this submission.

DATA AVAILABILITY

The *TESS* data is accessible via the MAST (Mikulski Archive for Space Telescopes) portal at <https://mast.stsci.edu/portal/Mashup/Clients/Mast/Portal.html>.

The *HARPS* data can be obtained from the ESO archive at <http://archive.eso.org/cms.html>

Any code used for analysis or in producing the plots in this paper can be made available upon reasonable request to the author(s).

REFERENCES

- Acton J. S., et al., 2020a, *MNRAS*, **494**, 3950
- Acton J. S., et al., 2020b, *MNRAS*, **498**, 3115
- Almeida-Fernandes F., Rocha-Pinto H. J., 2018, *MNRAS*, **476**, 184
- Baraffe I., Homeier D., Allard F., Chabrier G., 2015, *A&A*, **577**, A42
- Bayliss D., et al., 2020, *The Messenger*, **181**, 28
- Bayliss D., et al., 2022, in Holland A. D., Beletic J., eds, Society of Photo-Optical Instrumentation Engineers (SPIE) Conference Series Vol. 12191, X-Ray, Optical, and Infrared Detectors for Astronomy X. p. 121911A, doi:10.1117/12.2628966
- Bensby T., Feltzing S., Lundström I., 2003, *A&A*, **410**, 527
- Bensby T., Feltzing S., Oey M. S., 2014, *A&A*, **562**, A71
- Blanco-Cuaresma S., 2019, *MNRAS*, **486**, 2075
- Blanco-Cuaresma S., Soubiran C., Heiter U., Jofré P., 2014a, iSpec: Stellar atmospheric parameters and chemical abundances, Astrophysics Source Code Library, record ascl:1409.006
- Blanco-Cuaresma S., Soubiran C., Heiter U., Jofré P., 2014b, *A&A*, **569**, A111
- Börner A., et al., 2024, *Experimental Astronomy*, **58**, 1
- Bowler B. P., Blunt S. C., Nielsen E. L., 2020, *AJ*, **159**, 63
- Brahm R., Jordán A., Espinoza N., 2017, *PASP*, **129**, 034002
- Brahm R., et al., 2019, *AJ*, **158**, 45
- Brahm R., et al., 2023, *AJ*, **165**, 227
- Bryant E. M., et al., 2020, *MNRAS*, **494**, 5872
- Caldwell D. A., et al., 2020, *Research Notes of the American Astronomical Society*, **4**, 201
- Casewell S. L., et al., 2018, *MNRAS*, **481**, 1897
- Chabrier G., Gallardo J., Baraffe I., 2007, *A&A*, **472**, L17
- Chabrier G., Baraffe I., Phillips M., Debras F., 2023, *A&A*, **671**, A119
- Chen D.-C., et al., 2021, *ApJ*, **909**, 115
- Choi J., Dotter A., Conroy C., Cantiello M., Paxton B., Johnson B. D., 2016, *ApJ*, **823**, 102
- Claret A., Cunha N. C. S., 1997, *A&A*, **318**, 187
- Costa E., Mendez R. A., Jao W.-C., Henry T. J., Subasavage J. P., Ianna P. A., 2006, *The Astronomical Journal*, **132**, 1234
- Costes J. C., et al., 2021, *MNRAS*, **505**, 830
- Davis Y. T., et al., 2024, *MNRAS*,
- Dotter A., 2016, *ApJS*, **222**, 8
- Doyle L., Armstrong D. J., Bayliss D., Rodel T., Kunovac V., 2024, *MNRAS*, **529**, 1802
- Duck A., et al., 2023, *MNRAS*, **521**, 6305
- Eschen Y. N. E., Bayliss D., Wilson T. G., Kunimoto M., Pelisoli I., Rodel T., 2024, *arXiv e-prints*, p. arXiv:2409.13039
- Foreman-Mackey D., Hogg D. W., Lang D., Goodman J., 2013, *PASP*, **125**, 306
- Foreman-Mackey D., Agol E., Ambikasaran S., Angus R., 2017, *AJ*, **154**, 220
- Freckelton A. V., et al., 2024, *MNRAS*,
- Gaia Collaboration et al., 2021, *A&A*, **649**, A1
- Gill S., et al., 2019, *A&A*, **626**, A119
- Gill S., et al., 2020, *MNRAS*, **491**, 1548
- Gill S., et al., 2022, *MNRAS*, **513**, 1785
- Gillon M., et al., 2017, *Nature*, **542**, 456
- Gómez Maqueo Chew Y., et al., 2014, *A&A*, **572**, A50
- Gray R. O., Corbally C. J., 1994, *AJ*, **107**, 742
- Günther M. N., Daylan T., 2019, Allesfitter: Flexible Star and Exoplanet Inference From Photometry and Radial Velocity, Astrophysics Source Code Library (ascl:1903.003)
- Günther M. N., Daylan T., 2021, *ApJS*, **254**, 13
- Henden A., Munari U., 2014, Contributions of the Astronomical Observatory Skalnaté Pleso, **43**, 518
- Hilditch R. W., 2001, An Introduction to Close Binary Stars. Cambridge University Press, doi:10.1017/CBO9781139163576
- Hobson M. J., et al., 2021, *AJ*, **161**, 235
- Hoxie D. T., 1970, *ApJ*, **161**, 1083
- Huang C. X., et al., 2020, *Research Notes of the American Astronomical Society*, **4**, 206
- Husser T.-O., von Berg S. W., Dreizler S., Homeier D., Reiners A., Barman T., Hauschildt P. H., 2013, *Astronomy & Astrophysics*, **553**, A6
- Jackson B., Greenberg R., Barnes R., 2008, *ApJ*, **678**, 1396
- Jenkins J. S., et al., 2011, *A&A*, **531**, A8
- Jenkins J. S., et al., 2015, *Monthly Notices of the Royal Astronomical Society*, **453**, 1439
- Jenkins J. M., et al., 2016, in Chiozzi G., Guzman J. C., eds, Society of Photo-Optical Instrumentation Engineers (SPIE) Conference Series Vol. 9913, Software and Cyberinfrastructure for Astronomy IV. p. 99133E, doi:10.1117/12.2233418
- Jofré P., et al., 2014, *A&A*, **564**, A133
- Johnson D. R. H., Soderblom D. R., 1987, *AJ*, **93**, 864
- Jones M. I., et al., 2024, *arXiv e-prints*, p. arXiv:2401.09657
- Kaufer A., Stahl O., Tubbesing S., Nørregaard P., Avila G., Francois P., Pasquini L., Pizzella A., 1999, *The Messenger*, **95**, 8
- Keller S. C., et al., 2007, *Publ. Astron. Soc. Australia*, **24**, 1
- Kipping D. M., 2013, *MNRAS*, **435**, 2152
- Kraft R. P., 1967, *ApJ*, **150**, 551
- Kraft R. P., 1970, in Herbig G. H., Struve O., eds, Spectroscopic Astrophysics. An Assessment of the Contributions of Otto Struve. University of California Press, p. 385
- Kunovac Hodžić V., et al., 2020, *MNRAS*, **497**, 1627
- Kurucz R. L., 2005, *Memorie della Societa Astronomica Italiana Supplementi*, **8**, 14
- Lightkurve Collaboration et al., 2018, Lightkurve: Kepler and TESS time series analysis in Python, Astrophysics Source Code Library (ascl:1812.013)
- López-Morales M., 2007, *ApJ*, **660**, 732
- Lovis C., et al., 2011, *arXiv e-prints*, p. arXiv:1107.5325
- MacDonald J., Mullan D. J., 2014, *ApJ*, **787**, 70
- Mamajek E. E., Hillenbrand L. A., 2008, *ApJ*, **687**, 1264
- Macted P. F. L., 2016, *A&A*, **591**, A111
- Macted P. F. L., et al., 2022, *MNRAS*, **514**, 77
- Macted P. F. L., Triaud A. H. M. J., Martin D. V., 2023, *Universe*, **9**, 498
- Mayor M., et al., 2003, *The Messenger*, **114**, 20
- McLaughlin D. B., 1924, *ApJ*, **60**, 22
- Montalto M., et al., 2021, *A&A*, **653**, A98
- Morales J. C., Ribas I., Giménez Á., Baroch D., 2022, *Galaxies*, **10**, 98
- Morton T. D., 2015, isochrones: Stellar model grid package, Astrophysics Source Code Library, record ascl:1503.010
- Mullan D. J., MacDonald J., 2001, *ApJ*, **559**, 353
- Noyes R. W., Hartmann L. W., Baliunas S. L., Duncan D. K., Vaughan A. H., 1984, *ApJ*, **279**, 763
- Nutzman P., Charbonneau D., Irwin J., Burke C., Berta Z., Falco E. E., 2009, in AAS/Division for Planetary Sciences Meeting Abstracts #41. p. 8.02
- O’Brien S. M., et al., 2022, *MNRAS*, **509**, 6111
- Parsons S. G., et al., 2018, *MNRAS*, **481**, 1083

Parviainen H., Aigrain S., 2015, *MNRAS*, **453**, 3821

Pecaut M. J., Mamajek E. E., 2013, *ApJS*, **208**, 9

Queloz D., et al., 2001, *The Messenger*, **105**, 1

Rauer H., et al., 2014, *Experimental Astronomy*, **38**, 249

Reddy B. E., Lambert D. L., Allende Prieto C., 2006, *MNRAS*, **367**, 1329

Rein H., Liu S. F., 2012, *A&A*, **537**, A128

Rein H., Spiegel D. S., 2015, *MNRAS*, **446**, 1424

Ricker G. R., et al., 2015, *Journal of Astronomical Telescopes, Instruments, and Systems*, **1**, 014003

Rossiter R. A., 1924, *ApJ*, **60**, 15

Sbordone L., Bonifacio P., Castelli F., Kurucz R. L., 2004, *Memorie della Societa Astronomica Italiana Supplementi*, **5**, 93

Schlecker M., et al., 2020, *AJ*, **160**, 275

Sebastian D., et al., 2021, *A&A*, **645**, A100

Sebastian D., et al., 2023, *MNRAS*, **519**, 3546

Sebastian D., et al., 2024, *MNRAS*.

Skilling J., 2004, in Fischer R., Preuss R., Toussaint U. V., eds, *American Institute of Physics Conference Series Vol. 735, American Institute of Physics Conference Series*. pp 395–405, doi:10.1063/1.1835238

Skilling J., 2006, *Bayesian Anal.*, **1**, 833

Skrutskie M. F., et al., 2006, *AJ*, **131**, 1163

Smalley B., 2005, *Memorie della Societa Astronomica Italiana Supplementi*, **8**, 130

Smith G. D., et al., 2021, *MNRAS*, **507**, 5991

Soto M. G., Jenkins J. S., 2018, *A&A*, **615**, A76

Sousa S. G., Santos N. C., Adibekyan V., Delgado-Mena E., Israelian G., 2015, *A&A*, **577**, A67

Spada F., Demarque P., Kim Y. C., Sills A., 2013, *ApJ*, **776**, 87

Speagle J. S., 2020, *MNRAS*, **493**, 3132

Stanford-Moore S. A., Nielsen E. L., De Rosa R. J., Macintosh B., Czekala I., 2020, *ApJ*, **898**, 27

Stassun K. G., et al., 2019, *AJ*, **158**, 138

Swayne M. I., et al., 2021, *MNRAS*, **506**, 306

Swayne M. I., et al., 2024, *MNRAS*, **528**, 5703

Tayar J., Claytor Z. R., Huber D., van Saders J., 2022, *ApJ*, **927**, 31

TriAUD A. H. M. J., 2018, in Deeg H. J., Belmonte J. A., eds, , *Handbook of Exoplanets*. Springer International Publishing, Cham, p. 2, doi:10.1007/978-3-319-55333-7_2, https://doi.org/10.1007/978-3-319-55333-7_2

TriAUD A. H. M. J., et al., 2013, *A&A*, **549**, A18

TriAUD A. H. M. J., et al., 2017, *A&A*, **608**, A129

Trifonov T., et al., 2023, *AJ*, **165**, 179

Vines J. I., Jenkins J. S., 2022, *MNRAS*,

Watson C. A., Littlefair S. P., Collier Cameron A., Dhillon V. S., Simpson E. K., 2010, *MNRAS*, **408**, 1606

Wheatley P. J., et al., 2018, *MNRAS*, **475**, 4476

Winn J. N., 2014, in Seager S., ed., , *Exoplanets*. University of Arizona Press, pp 55–77, doi:10.48550/arXiv.1001.2010

Wright E. L., et al., 2010, *AJ*, **140**, 1868

Yan Y., Du C., Liu S., Li H., Shi J., Chen Y., Ma J., Wu Z., 2019, *ApJ*, **880**, 36

Yee S. W., Petigura E. A., von Braun K., 2017, *ApJ*, **836**, 77

von Boetticher A., et al., 2017, *A&A*, **604**, L6

von Boetticher A., et al., 2019, *A&A*, **625**, A150

APPENDIX A: allesfitter RESULTS TABLES**APPENDIX B: HARPS MASKED REGIONS****APPENDIX C: allesfitter PLOTS****APPENDIX D: isochrones PLOTS****APPENDIX E: TESS RAW LIGHTCURVES****APPENDIX F: THE NGTS-EB NAMING CONVENTION**

We have created the *NGTS-EB* naming system to describe eclipsing binary systems discovered by the Next Generation Transit Survey (*NGTS*; Wheatley et al. 2018). This naming system has been registered with the International Astronomical Union (IAU) Dictionary of Nomenclature of Celestial Objects³. The Acronym *NGTS-EB* stands for Next Generation Transit Survey - Eclipsing Binary and the naming convention follows the format *NGTS-EB-NNN A* where *NNN* is a sequential number given to each system and *A* and *B* denote the individual components of the system with *A* typically being the more massive component. We designate the system that is the focus of this paper *NGTS-EB-7*. Despite being the first object to receive an *NGTS-EB* moniker, we give it the number 7 as six previous eclipsing binary systems have been discovered by *NGTS*, which we retroactively give *NGTS-EB* numbers as shown in Table F1.

This paper has been typeset from a $\text{\TeX}/\text{\LaTeX}$ file prepared by the author.

³ Available at: <https://cds.unistra.fr/cgi-bin/Dic?NGTS-EB>

Table A1. allessfitter global model priors and fitted parameters.

Parameter	Initial guess	Prior	Fitted value	units
R_B/R_A	0.0893259057224787	$\mathcal{U}(0.07, 0.14)$	$0.0869^{+0.0012}_{-0.0011}$	
$(R_A + R_B)/a_B$	0.0113578760330941	$\mathcal{U}(0.008, 0.05)$	$0.01098^{+0.00026}_{-0.00016}$	
$\cos i_B$	0.0057874459294714	$\mathcal{U}(0, 1.0)$	$0.0032^{+0.0028}_{-0.0021}$	
$T_{0:B}$	2459486.073495738	$\mathcal{U}(2459485.5, 2459486.5)$	$2459486.0746^{+0.0016}_{-0.0015}$	bjd
P_B	193.3585642579528	$\mathcal{U}(192.0, 194.0)$	193.35875 ± 0.00034	d
$\sqrt{e_B} \cos \omega_B$	-0.835487	$\mathcal{U}(-1.0, 1.0)$	-0.83371 ± 0.00076	
$\sqrt{e_B} \sin \omega_B$	0.131535	$\mathcal{U}(-1.0, 1.0)$	0.1389 ± 0.0028	
K_B	4.651554575593812	$\mathcal{U}(0.0, 12.0)$	4.6150 ± 0.0096	km/s
dilution TESS8	0.02864754	Fixed		
dilution TESS29	0.0140216899999999	Fixed		
$q_{1:NGTS}$	0.37	$\mathcal{N}(0.37, 0.01)$	0.375 ± 0.010	
$q_{1:NGTS}$	0.40	$\mathcal{N}(0.40, 0.08)$	0.401 ± 0.078	
$q_{1:TESS8}$	0.315	$\mathcal{N}(0.315, 0.008)$	0.3149 ± 0.0083	
$q_{2:TESS8}$	0.39	$\mathcal{N}(0.39, 0.08)$	0.379 ± 0.069	
$q_{1:TESS29}$	0.315	$\mathcal{N}(0.315, 0.008)$	0.3152 ± 0.0083	
$q_{2:TESS29}$	0.39	$\mathcal{N}(0.39, 0.08)$	0.396 ± 0.073	
$\log \sigma_{TESS8}$	-7.31	$\mathcal{N}(-7.31, 0.04)$	$-7.130^{+0.090}_{-0.085}$	log(rel.flux.)
$\log \sigma_{TESS29}$	-6.54	$\mathcal{N}(-6.54, 0.02)$	-7.310 ± 0.021	log(rel.flux.)
$\log \sigma_{NGTS}$	-7.4	$\mathcal{N}(-7.4, 0.7)$	-6.527 ± 0.011	log(rel.flux.)
$\log \sigma_{CORALIE}$	-5.0	$\mathcal{U}(-7.6, -1.6)$	$-3.99^{+0.42}_{-0.69}$	log(km/s)
$\log \sigma_{HARPS}$	-6.0	$\mathcal{U}(-7.6, -1.6)$	$-4.27^{+0.27}_{-0.25}$	log(km/s)
$\log \sigma_{FEROS}$	-5.0	$\mathcal{U}(-7.6, -1.6)$	-3.48 ± 0.29	log(km/s)
GP ln σ (TESS8)	-7.7	$\mathcal{N}(-7.7, 0.4)$	$-7.50^{+0.20}_{-0.18}$	
GP ln ρ (TESS8)	0.3	$\mathcal{N}(0.3, 0.6)$	0.07 ± 0.27	
GP ln σ (TESS29)	-7.01	$\mathcal{N}(-7.01, 0.08)$	-7.009 ± 0.052	
GP ln ρ (TESS29)	-1.79	$\mathcal{N}(-1.7, 0.2)$	-1.714 ± 0.099	
offset CORALIE	78.71	$\mathcal{N}(78.71, 0.95)$	78.4273 ± 0.0089	km/s
offset HARPS	78.71	$\mathcal{N}(78.71, 0.95)$	78.3140 ± 0.0064	km/s
offset FEROS	78.71	$\mathcal{N}(78.71, 0.95)$	$78.418^{+0.010}_{-0.011}$	km/s

Table A2. System derived parameters.

Derived parameter	Value
Host radius over semi-major axis B; R_A/a_B	$0.01011^{+0.00023}_{-0.00014}$
Semi-major axis B over host radius; a_B/R_A	$98.9^{+1.4}_{-2.2}$
Companion radius B over semi-major axis B; R_B/a_B	$0.000878^{+0.000026}_{-0.000018}$
Companion radius B; $R_B (R_\oplus)$	13.66 ± 0.65
Companion radius B; $R_B (R_{Jup})$	1.219 ± 0.058
Semi-major axis B; $a_B (R_\odot)$	142.0 ± 7.1
Semi-major axis B; $a_B (AU)$	0.661 ± 0.033
Inclination B; $i_B (deg)$	$89.82^{+0.12}_{-0.16}$
Eccentricity B; e_B	0.71436 ± 0.00085
Argument of periastron B; $w_B (deg)$	$170.54^{+0.20}_{-0.19}$
Mass ratio B; q_B	$0.0952^{+0.0055}_{-0.0049}$
Companion mass B; $M_B (M_\oplus)$	35700^{+2900}_{-2700}
Companion mass B; $M_B (M_{Jup})$	$112.3^{+9.2}_{-8.5}$
Companion mass B; $M_B (M_\odot)$	$0.1072^{+0.0088}_{-0.0082}$
Impact parameter B; $b_{tra:B}$	$0.138^{+0.12}_{-0.090}$
Total transit duration B; $T_{tot:B} (h)$	$10.06^{+0.11}_{-0.10}$
Full-transit duration B; $T_{full:B} (h)$	$8.406^{+0.092}_{-0.099}$
Companion density B; $\rho_B (cgs)$	77^{+17}_{-14}
Companion surface gravity B; $g_B (cgs)$	157400^{+6600}_{-9000}
Equilibrium temperature B; $T_{eq:B} (K)$	375.7 ± 8.6
Combined host density from all orbits; $\rho_{A:combined} (cgs)$	$0.490^{+0.022}_{-0.032}$

Table A3. Instrumental derived parameters.

Derived parameter	Value
Transit depth (undil.) B; $\delta_{tr,undil:B;TESS8} (ppt)$	$8.97^{+0.25}_{-0.22}$
Transit depth (dil.) B; $\delta_{tr,dil:B;TESS8} (ppt)$	$8.71^{+0.24}_{-0.22}$
Transit depth (undil.) B; $\delta_{tr,undil:B;TESS29} (ppt)$	9.01 ± 0.25
Transit depth (dil.) B; $\delta_{tr,dil:B;TESS29} (ppt)$	8.89 ± 0.25
Transit depth (undil.) B; $\delta_{tr,undil:B;NGTS} (ppt)$	$9.17^{+0.33}_{-0.29}$
Transit depth (dil.) B; $\delta_{tr,dil:B;NGTS} (ppt)$	$9.17^{+0.33}_{-0.29}$
Limb darkening; $u_{1:TESS8}$	0.424 ± 0.078
Limb darkening; $u_{2:TESS8}$	0.136 ± 0.078
Limb darkening; $u_{1:TESS29}$	0.444 ± 0.083
Limb darkening; $u_{2:TESS29}$	0.117 ± 0.083
Limb darkening; $u_{1:NGTS}$	0.491 ± 0.096
Limb darkening; $u_{2:NGTS}$	0.121 ± 0.096

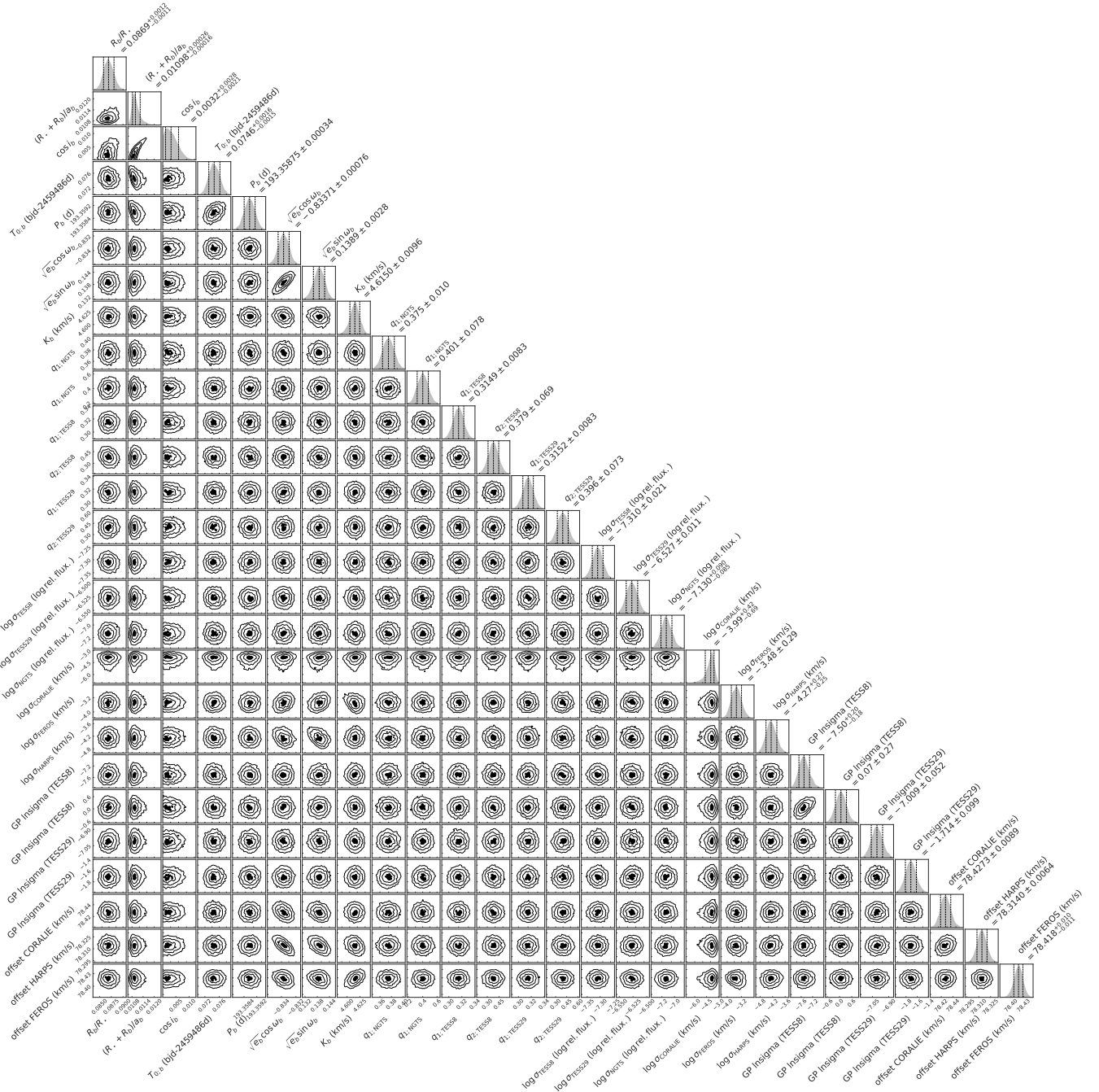


Figure C1. Corner plot of fitted parameters from the allesfitter global model.

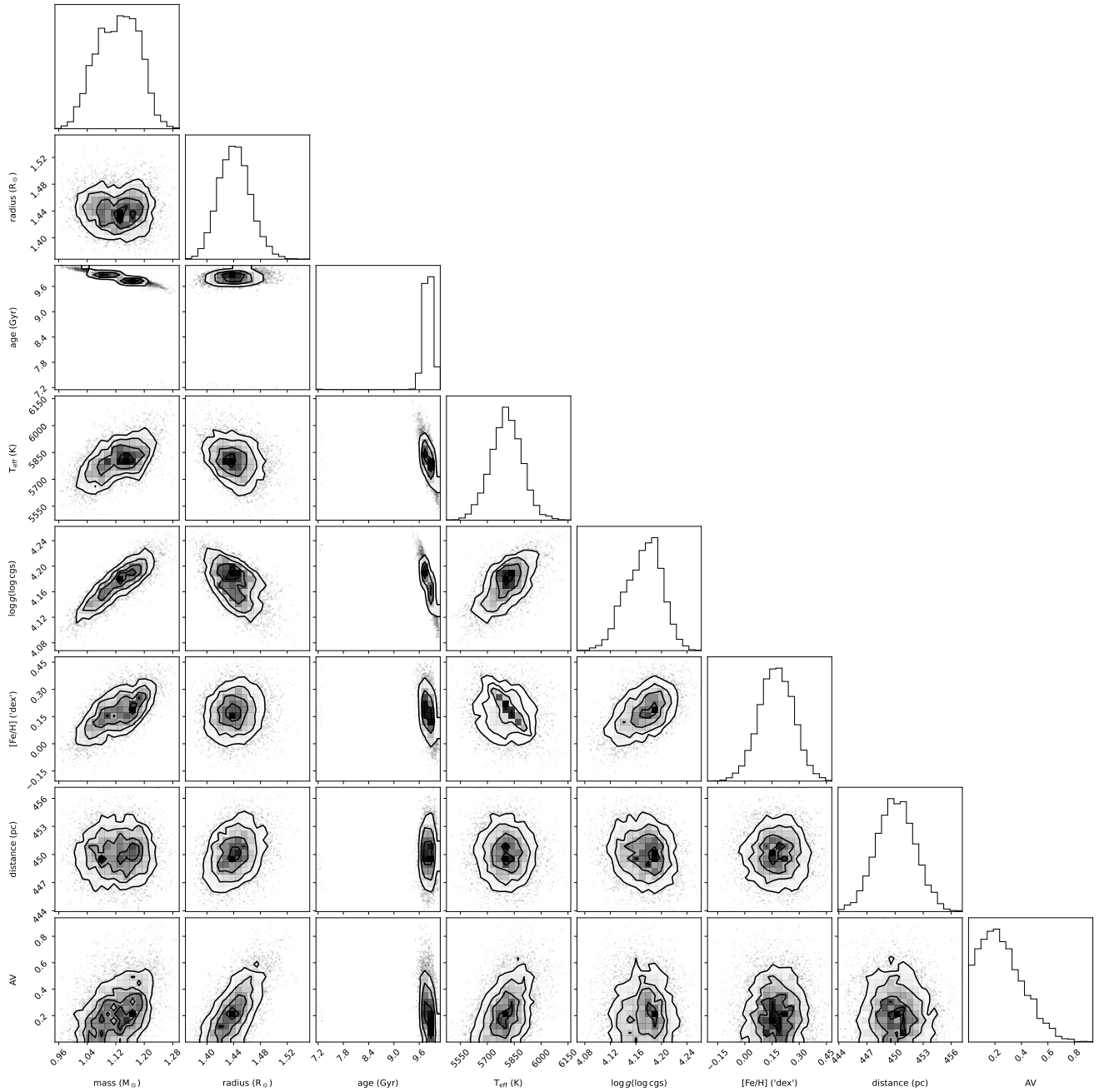


Figure D1. Corner plot of physical parameters from isochrones using priors from PAWS.

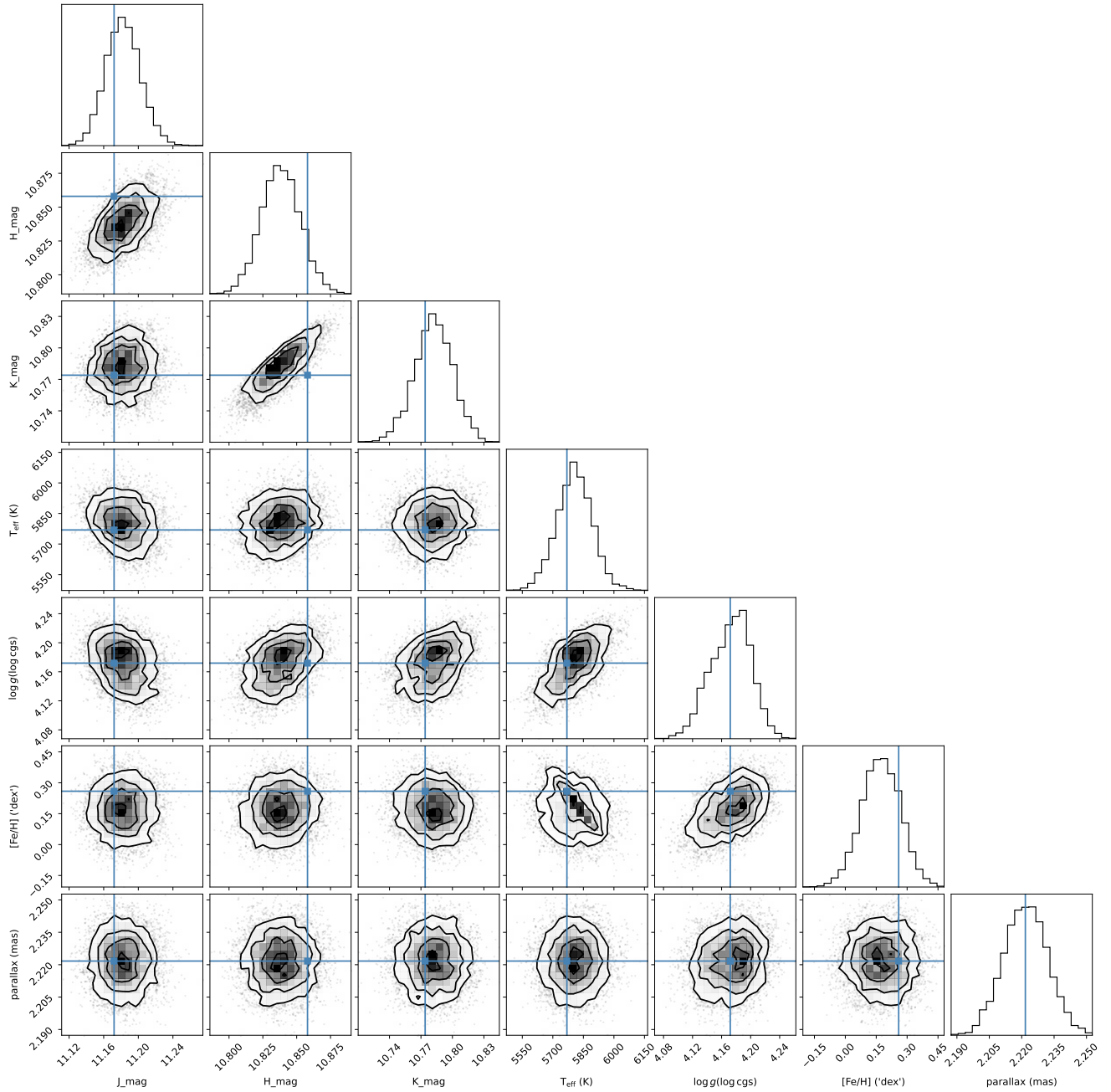


Figure D2. Corner plot of observables from isochrones using priors from PAWS.

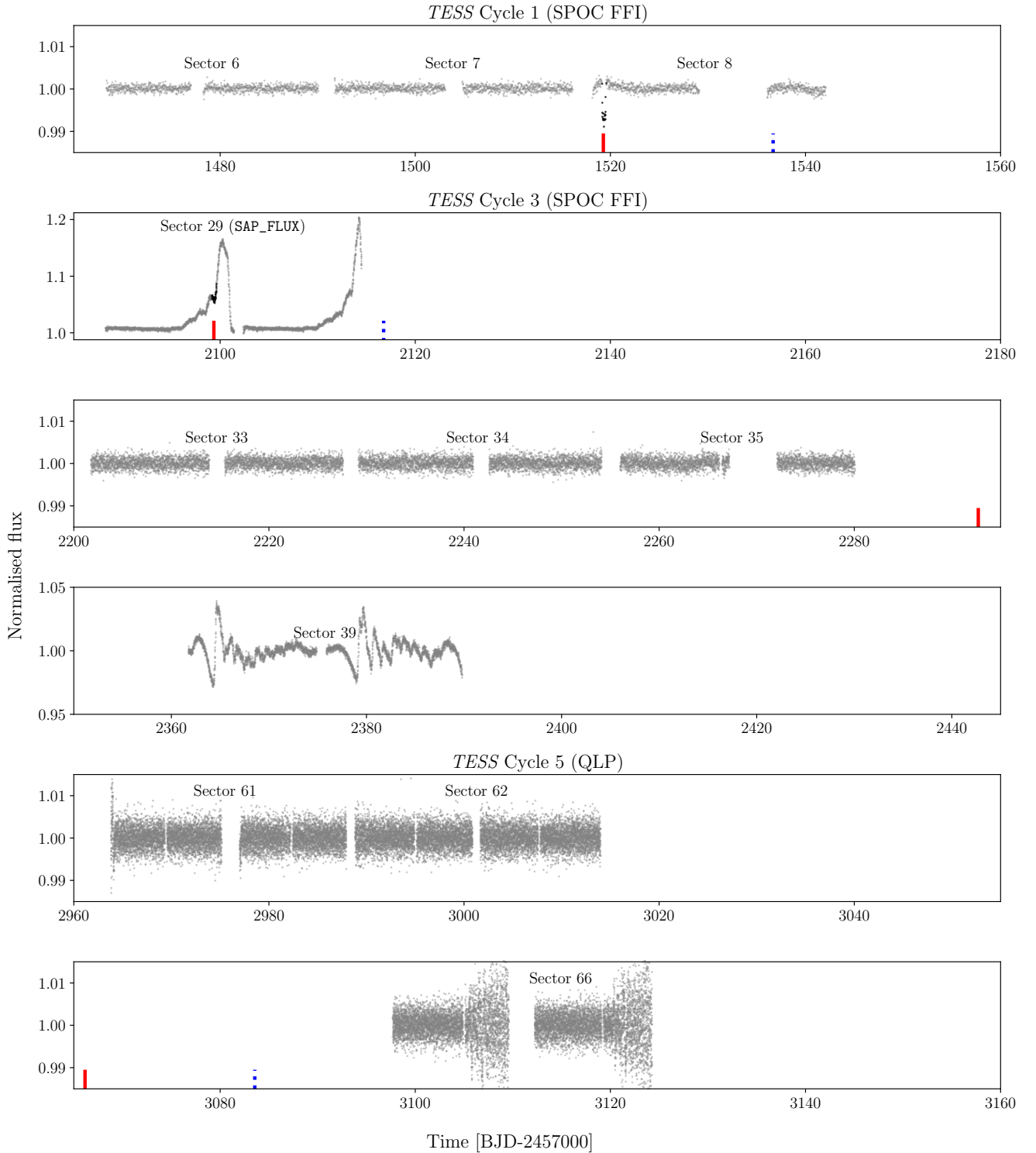


Figure E1. All *TESS* lightcurves for *NGTS-EB-7* plotted in grey with transits marked by red vertical lines, secondary eclipses with blue dotted vertical lines and in-transit data-points are highlighted black. Each panel shows a time-span of 95 days so that all the transits happening within each *TESS* cycle can be seen. The top panel represents Cycle 1, the middle three show Cycle 3 and the bottom two Cycle 5. For Sectors 6-8 and 33-39 we plot the PDCSAP_FLUX flux from the SPOC FFI lightcurves while for Sector 29 we plot the SAP_FLUX. The lightcurves for sectors 61-66 are sourced from the Quick Look Pipeline (QLP; [Huang et al. 2020](#)) and the detrended DET_FLUX.

Table B1. *HARPS* masked wavelength ranges.

Wavelength range (nm)	Wavelength range (nm)
390.40-390.50	488.87-489.12
390.99-391.16	492.84-493.15
392.26-392.33	498.14-498.43
392.83-392.85	508.68-509.00
395.94-396.12	514.43-514.75
399.27-399.49	519.40-519.45
402.60-402.78	522.87-522.91
405.87-406.06	529.83-529.87
408.94-408.95	534.45-534.50
409.10-409.30	545.10-545.16
411.10-411.15	552.15-552.37
418.50-418.75	557.70-557.75
422.15-422.35	562.46-562.50
425.74-425.92	566.89-567.14
431.98-432.02	582.38-582.43
433.78-433.80	582.60-583.05
435.05-435.08	583.34-583.38
436.10-436.40	598.04-598.50
438.16-438.18	599.30-599.34
440.25-440.05	599.98-600.70
441.31-441.35	601.83-602.34
444.29-444.35	603.85-604.34
444.51-444.55	605.99-606.62
446.59-446.63	607.88-608.30
447.75-447.80	609.17-610.38
451.05-451.10	618.50-619.30
455.97-456.26	629.84-630.20
456.31-456.35	637.16-637.20
460.32-460.70	637.58-637.60
460.80-460.85	647.91-648.05
473.37-473.70	652.19-652.22
478.31-478.46	676.99-677.03
483.06-483.25	

Table F1. *NGTS-EB* systems.

<i>NGTS-EB</i> #	Original designation	TICID	<i>Gaia</i> DR3 ID	2MASS ID	RA	DEC	Reference
1	<i>NGTS</i> J052218.2-250710.4	31054255	2957804068198875776	J05221817-2507112	5 ^h 22 ^m 18.17 ^s	−25°07′10.80″	1
2	<i>NGTS</i> J214358.5-380102	197570458	6586032117320121856	J21435859-3801027	21 ^h 43 ^m 58.59 ^s	−38°1′3.41″	2
3	TIC 231005575	231005575	4912474299133826560	J01400127-5431218	1 ^h 40 ^m 1.35 ^s	−54°31′21.99″	3
4	<i>NGTS</i> J0930-18	176772671	5678383069566263552	J09301604-1850353	9 ^h 30 ^m 16.00 ^s	−18°50′35.03″	4
5	<i>NGTS</i> J0002-29	313934158	2320868389659322368	J00024841-2953539	0 ^h 2 ^m 48.45 ^s	−29°53′53.89″	5
6	TIC 320687387	320687387	6641131183310690432	J19511834-5532469	19 ^h 51 ^m 18.41 ^s	−55°32′47.50″	6
7	<i>NGTS-EB-7</i>	238060327	5504617415848984320	J06564704-5204263	6 ^h 56 ^m 47.04 ^s	−52°04′26.11″	This work

References: 1:[Casewell et al. \(2018\)](#), 2:[Acton et al. \(2020a\)](#), 3:[Gill et al. \(2020\)](#), 4: [Acton et al. \(2020b\)](#), 5:[Smith et al. \(2021\)](#), 6:[Gill et al. \(2022\)](#).